2016

Terahertz and mid-infrared photodetectors based on intersubband transitions in novel materials systems

https://hdl.handle.net/2144/17077

Boston University

BOSTON UNIVERSITY

COLLEGE OF ENGINEERING

Dissertation

TERAHERTZ AND MID-INFRARED PHOTODETECTORS BASED ON INTERSUBBAND TRANSITIONS IN NOVEL MATERIALS SYSTEMS

by

HABIBE DURMAZ

B.S., Selcuk University, 2006
M.S., Temple University, 2010

Submitted in partial fulfillment of the

requirements for the degree of

Doctor of Philosophy

2016

Approved by

First Reader ______________________________

Roberto Paiella, Ph.D.
Professor of Electrical and Computer Engineering
Professor of Materials Science and Engineering

Second Reader ______________________________

Theodore Moustakas, Ph.D.
Distinguished Professor Emeritus of Photonics and Optoelectronics
Professor Emeritus of Electrical and Computer Engineering
Professor Emeritus of Materials Science and Engineering
Professor Emeritus of Physics

Third Reader ______________________________

Enrico Bellotti, Ph.D.
Professor of Electrical and Computer Engineering
Professor of Materials Science and Engineering

Fourth Reader ______________________________

Anna Swan, Ph.D.
Associate Professor of Electrical and Computer Engineering
Associate Professor of Materials Science and Engineering

To my family

DEDICATION

I would like to dedicate this work to my family and loved ones
who have inspired me all my life.

ACKNOWLEDGMENTS

First and foremost, I would like to thank to my advisor Professor Roberto Paiella for his continuous support of my research. It is impossible to express my gratitude to him in a few short lines. I'm really thankful for the excellent research opportunities that Prof. Paiella provided me during my Ph.D. I feel very lucky to be supervised by him and am honored to have worked in his research group. He is an excellent and an outstanding teacher and advisor who passed his knowledge, experience, and wisdom to us very effectively. It was also a great opportunity to attend his lectures and to learn from him not only science but also teaching experience.

I would like to thank Professor Theodore Moustakas, Professor Enrico Bellotti and Professor Anna Swan for spending their valuable time and effort on evaluating my thesis and being on my committee. I really appreciate their advice and academic suggestions. I would like to further thank to Prof. Moustakas for giving me the opportunity to collaborate with him. It is such an honor and privilege to meet him in my academic career and also do research with him besides attending all his wonderful lectures. I could not have imagined having a better teacher and mentor during my school life. I also want to give my special thanks to Prof. Bellotti for giving all the motivation towards graduation and the classes that helped for the completion of this thesis work. I will always remember his motivations, suggestions not only for academia but also for life. I still remember him saying "Go home!" whenever he saw me working late hours. I want to express my thanks to Prof. Swan for collaboration work on graphene project, all discussions in our meetings, and being a successful role model in academia as female professor for prospective female academician. It is an honor to know her as guide for my future academic life.

I would like to give my special thanks to my colleagues in the Semiconductors photonics group. Special thanks to Faisal for passing all the experience and knowledge on THz project. I would like thanks to our former and current group members: Cicek, Jeff, Khwanchai, Kogos, Sunami, Xiaowei and Yuyu for many technical helps and general discussions.

I also would like to thank to Wide Bandgap Semiconductor Lab members; Denis, Gordie, and Wei for the growth and characterization of the samples, especially Denis for trying really hard to grow a Quantum Well structure on a semi-polar Galium Nitride (GaN) sample. I would like to thank my collaborators in Professor Max Lagally's group at the University of Wisconsin at Madison, in particular Pornsatit Sookchoo who grew many Silicon Germanium nanomembrane (SiGe NM) samples with countless effort and patient.

I would like to thank my friends in Boston; Fatma Zehra, Sevtap, Gul, Khwanchai, Beyza, Yasin, and Romeissa for giving me the family comfort and sharing their true friendship.

Finally and most importantly, I want to reserve my very special thanks to my family for being with me despite the long distance. I am very grateful for the unconditional love and support from my parents, my siblings, and nieces-and- nephews throughout my life. Special thanks to my lovely niece Beyza who always makes me smile and gives a cheerful joy during this stressful journey. One special person I want to give my special thanks is my best and childhood friend Sinan who always supports me unconditionally in any aspect of my life.

TERAHERTZ AND MID-INFRARED PHOTODETECTORS BASED ON INTERSUBBAND TRANSITIONS IN NOVEL MATERIALS SYSTEMS

HABIBE DURMAZ

Boston University College of Engineering, 2016

Major Professor: Roberto Paiella, Ph.D., Professor of Electrical and Computer Engineering, Professor of Materials Science and Engineering

ABSTRACT

The terahertz (THz) and mid-infrared (MIR) spectral regions have many potential applications in the industrial, biomedical, and military sectors. Yet, a wide portion of this region of the electromagnetic spectrum (particularly the THz range) is still relatively unexplored, due mainly to the absence of suitable sources and photodetectors, related to the lack of practical semiconductor materials with adequately small band gap energies. Intersubband transitions (ISBTs) between quantized energy states in quantum heterostructures provide tunable wavelengths over a broad spectral range including the THz region, by choosing appropriate layer thicknesses and compositions.

This work focuses on the development of THz and MIR Quantum Well Infrared Photodetectors (QWIPs) based on ISBTs in GaN/AlGaN and Si/SiGe heterostructures. Due to their large optical phonon energies, GaN materials allow extending the spectral reach of existing far-infrared photodetectors based on GaAs, and may enable higher-temperature operation. In the area of MIR optoelectronic devices, I have focused on developing QWIPs based on ISBTs in Si/SiGe heterostructures in the form of on strain-engineered nanomembranes. Due to their non-polar nature, these materials are free from reststrahlen absorption and ultrafast resonant electron/phonon scattering, unlike traditional III-V semiconductors. Therefore, Si/SiGe quantum wells (QWs) are also promising candidates for high-temperature high-performance ISB device operation (particularly in the THz region), with the additional advantage of direct integration with CMOS technology.

In this thesis work, numerical modeling is used to design the active region of the proposed devices, followed by sample fabrication and characterization based on lock-in step-scan Fourier transform infrared spectroscopy. Three specific QWIP devices have been developed. The first is a III-nitride THz QWIP based on a novel double-step QW design in order to alleviate the material limitations provided by the intrinsic electric fields of GaN/AlGaN heterostructures. Next, I have developed a THz GaN/AlGaN QWIP grown on semi-polar $(20\bar{2}\bar{1})$ GaN, where the detrimental effects of the internal fields are almost completely eliminated. Finally, I have demonstrated a Si/SiGe MIR QWIP based on a novel fabrication approach, where nanomembrane strain engineering is used to address the materials quality issues normally found in SiGe QWs. Promising photodetector performance is obtained in all cases.

TABLE OF CONTENTS

LIST OF FIGURES

LIST OF ABBREVIATIONS

2D	Two Dimensional
AlAsSb	Aluminum Arsenide Antimonide
AlGaAs	Aluminum Gallium Arsenide
AlGaN	Aluminum Gallium Nitride
AlN	Aluminum Nitride
BOX	Buried Oxide
CMOS	Complementary Metal Oxide Semiconductor
EBL	Electron Beam Lithography
FIR	Far-Infrared
FWHM	Full Width at Half Maximum
GaAs	Gallium Arsenide
GaN	Gallium Nitride
Ge	Germanium
GeSn	Germanium Tin
HH	Heavy Hole
ICP-RIE	Inductively Coupled Plasma-Reactive Ion Etching
InAlAs	Indium Aluminum Arsenide
InGaAs	Indium Gallium Arsenide
InGaAsP	Indium Gallium Arsenide Phosphide
InP	Indium Phosphide
InPAs	Indium Phosphide Arsenide

ISB	Intersubband
LED	Light Emitting Diode
LH	Light Hole
LO	Longitudinal Optical
MBE	Molecular Beam Epitaxy
MIR	Mid-Infrared
MQW	Multiple Quantum Well
NM	Nanomembrane
PL	Photoluminescence
PMMA	Poly(methyl-methacrylate)
QC	Quantum Cascade
QW	Quantum Well
QWIP	Quantum Well Infrared Photodetectors
RIE	Reactive Ion Etching
SEM	Scanning Electron Microscope
Si	Silicon
SiGe	Silicon Germanium
SOI	Silicon on Insulator
TE	Transverse Electric
THz	Terahertz
TM	Transverse Magnetic

1 INTRODUCTION

Terahertz light consists of electromagnetic waves with frequency between 300 GHz and 10 THz, at the boundary between the infrared and microwave parts of the spectrum. These waves can propagate through materials that are usually opaque to both visible and infrared radiation. Therefore, they are an ideal imaging and screening tool for industrial quality control, security screening, biometrics, medical imaging, and spectroscopic sensing (e.g., for explosive and illicit material detection) (Tonouchi 2006; Soref 2010; J. M. Chamberlain 2007; Hassan et al. 2012; C. H. Zhang et al. 2012; Norbert Palka 2013; Grossman et al. 2010; Miller, Luukanen, and Grossman 2004). The lack of semiconductor materials with sufficiently small bandgap energy makes intersubband transitions (ISBTs) in semiconductor heterostructures particularly promising for the development of THz devices (H. C. Liu and F Capasso 2000; R. Paiella 2006). Intersubband transitions refer to electronic transitions in low-dimensional semiconductors involving quantized states within the same energy band. As opposed to interband devices, the operating wavelength of ISB devices is determined by the layer thicknesses and alloy compositions and it is not fixed by the semiconductor material band structure. As a result, the transition energies of ISB devices are not directly limited by the bandgap properties of the underlying materials.

In this dissertation work, I have studied GaN/AlGaN and Si/SiGe quantum wells (QWs) for THz optoelectronic device applications, particularly quantum well infrared photodetectors (QWIPs). Chapter 2 presents a brief theoretical overview of ISBTs in the conduction band (which are relevant for the GaN/AlGaN materials system) and in the valence bands (as relevant for the Si/SiGe materials system), together with the basic principles of QWIP design and optimization. The design, fabrication, and electrical and optical characterization of a GaN/AlGaN QWIP grown on c-plane GaN and based on a novel double-step QW design are described in Chapter 3. Chapter 4 is focused on the development of a GaN/AlGaN THz QWIP grown on a semi-polar GaN substrate. This section includes a discussion of the theoretical model that I have developed in order to design the active region of these structures. The development of THz Si/SiGe QW structures based on nanomembrane (NM) strain engineering and the measurement of their absorption properties are presented in Chapter 5. Si/SiGe NM QWIPs have also been developed in this thesis work, as described in Chapter 6. Finally, conclusions and future directions are presented in the final section.

2 INTRODUCTION TO INTERSUBBAND TRANSITIONS

2.1 Background Information

Intersubband transitions (ISBTs) refer to electronic transitions between confined states within either the conduction band (n-type) or the valence bands (p-type) in QW structures. A QW is formed by a thin layer of a narrower-bandgap semiconductor (A) sandwiched between two barrier layers consisting of a wider-bandgap semiconductor (B). The motion of the charge carriers perpendicular to these layers becomes quantized, so that localized two-dimensional (2-D) subbands of quantized states are formed inside the QW. The resulting conduction-band structure is shown in Figure 2.1. The thickness of the well layer (A) determines the energy levels E_{c1}, E_{c2}, etc., and the well and barrier compositions determine the conduction band-offset ΔE_c, i.e., the QW depth. Every QW supports at least one bound ground state, and possibly one or more excited states depending on the thickness and compositions. Incident light can then be absorbed in this system through the excitation of electrons from the ground state to a higher-energy subband, via ISB optical transitions. In the following subsections, I will give an introduction to these transitions in both the conduction and the valence bands.

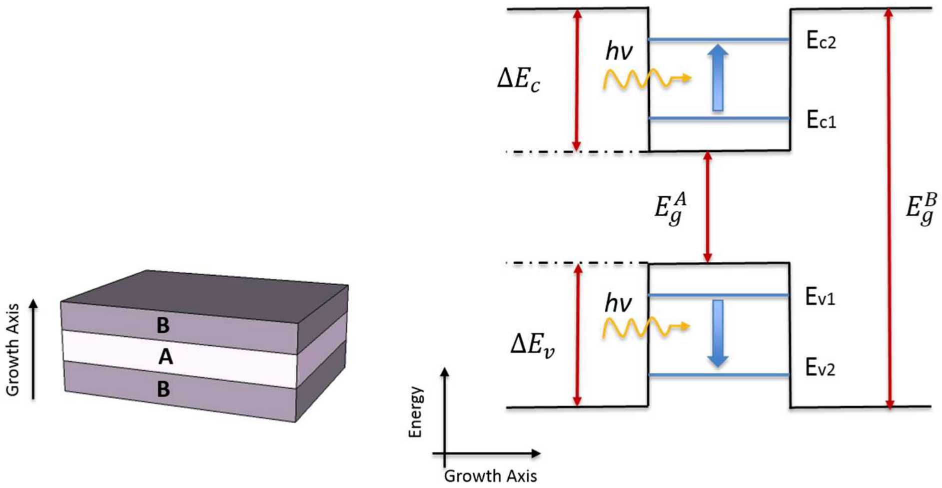

Figure 2.1 (a) Heterostructure consisting of a thin layer A sandwiched between thicker layers of material B. (b) Conduction-band diagram of the same heterostructure.

2.1.1 Intersubband Transitions in the Conduction Band

In order to design optimized QW structures for ISB device applications, we have developed a self-consistent Poisson and Schrodinger equations solver. This numerical code computes the conduction-band energy profile and the bound-state energy levels and envelope functions within the effective mass approximation, which is briefly reviewed in the following. A semiconductor crystal consists of periodically arranged atoms, resulting in a periodic potential. According to the effective-mass approximation, the total wave function of an electron in a QW structure is given by

$$\psi_{n,\mathbf{k}_{||}}(\mathbf{r}) = F_{n,\mathbf{k}_{||}}(\mathbf{r}) U_c(\mathbf{r}) \tag{2.1}$$

where n is the subband index, $F_{n,\mathbf{k}_{||}}(\mathbf{r})$ is the slowly-varying envelope function, $U_c(\mathbf{r})$ is the rapidly-varying lattice periodic Bloch function of the conduction band, and $\mathbf{k}_{||} = k_x\hat{\mathbf{x}} + k_y\hat{\mathbf{y}}$ is a two-dimensional wavevector on the plane of the QW.

For free motion in the x and y directions (with z being the growth direction), the envelope function can be written as

$$F_{n,\mathbf{k}_{||}}(\mathbf{r}) = \frac{1}{\sqrt{A}} e^{i\mathbf{k}_{||}.\mathbf{r}} \varphi_{n,\mathbf{k}_{||}}(z) \tag{2.2}$$

where A is the sample area. Inserting equation (2.1) in the Schrodinger equation, we get

$$\left[-\frac{\hbar^2}{2}\nabla.\frac{1}{m_c(\mathbf{r})}\nabla + V_c(\mathbf{r}) + V_{ext}(\mathbf{r})\right] F_{n,k_{||}}(\mathbf{r}) = E_n(\mathbf{k}_{||}) F_{n,k_{||}}(\mathbf{r}) \tag{2.3}$$

where m_c is the position-dependent electron effective mass, V_c is the conduction-band-edge energy, and V_{ext} is an external potential. In our simulations, the external potential is due to the bias voltage applied on the entire structure. Substituting equation (2.2) in equation (2.3) gives the one-dimensional Schrodinger equation

$$\left[-\frac{\hbar^2}{2}\frac{d}{dz}\frac{1}{m_c(z)}\frac{d}{dz} + \frac{\hbar^2 k_{||}^2}{2m_c(z)} + V_c(z) + V_{ext}(z)\right] \varphi_{n,\mathbf{k}_{||}}(z) = E_n\left(k_{||}\right) \varphi_{n,\mathbf{k}_{||}}(z) \tag{2.4}$$

In any multiple-QW (MQW) structure, such as the active material of a QWIP, equation (2.4) needs to be solved in each layer, and the boundary conditions at the interfaces $z=z_{AB}$,

$$\varphi_n^A(z_{AB}) = \varphi_n^B(z_{AB}) \qquad \text{and} \qquad \frac{1}{m_c^A}\frac{d\varphi_n^A}{dz}(z_{AB}) = \frac{1}{m_c^B}\frac{d\varphi_n^B}{dz}(z_{AB}) \tag{2.5}$$

must then be applied. With this procedure, one can find the z-dependent envelope functions $\varphi_{n,\mathbf{k}_{||}}(z)$ and the corresponding energy dispersion relations

$$E_n\left(\mathbf{k}_{||}\right) = E_n + \frac{\hbar\left(k_x^2 + k_y^2\right)}{2m_c} \tag{2.6}$$

where E_n is minimum energy of the n-th subband.

Since QWIPs are based on ISB absorption in QWs, their design requires computing the ISB absorption coefficient, which can be done using Fermi’s golden rule. The transition rate W_{if} from an initial state $|\psi_i\rangle$ to a final state $|\psi_f\rangle$ under the influence of an external electromagnetic wave of frequency ω is given by:

$$W_{if} = \frac{2\pi}{\hbar}|\langle\psi_i|H'|\psi_f\rangle|^2\delta(E_f - E_i - \hbar\omega) \tag{2.7}$$

where $H' = \frac{e}{2m_c}(\mathbf{A}.\mathbf{p} + \mathbf{p}.\mathbf{A})$ is the electron-photon interaction Hamiltonian. In this expression, **p** is the momentum operator and **A** is the vector potential of the electromagnetic wave. More details of this calculation can be found in Helm (Helm 2000). In general, the characteristic length of the electronic wavefunctions (the QW thickness ≈ 5-200 Å in the case of ISBTs) is much smaller than the radiation wavelength (1-50 μm), and as a result the Hamiltonian can be approximated by $H' = \frac{e}{m_c}\mathbf{A_o}.\mathbf{p}$, where $\mathbf{A_o}$ is the complex amplitude of the vector potential, which is proportional to the polarization unit vector **e**. Therefore, equation (2.7) can be written as:

$$W_{if} = \frac{2\pi}{\hbar}\frac{e^2E_0^2}{m_c^2w^2}|\langle\psi_i|\mathbf{e}.\mathbf{p}|\psi_f\rangle|^2\delta(E_f - E_i - \hbar w) \tag{2.8}$$

Inserting ψ_i and ψ_f in equation (2.7) based on equation (2.1), the matrix element $\langle\psi_i|\mathbf{e}.\mathbf{p}|\psi_f\rangle$ can be split in two parts due to the slower variations of the envelope function $F_{n,\mathbf{k}||}$ as compared to the Bloch function U_c, i.e.,

$$\langle\psi_i|\mathbf{e}.\mathbf{p}|\psi_f\rangle = \mathbf{e}.\langle U_c|\mathbf{p}|U_c\rangle\langle f_n|f_n'\rangle + \mathbf{e}.\langle U_c|U_c\rangle\langle f_n|\mathbf{p}|f_n'\rangle \tag{2.9}$$

Due to the symmetry properties of the Bloch-periodic function $\mathrm{U_c}$, the first term vanishes. ISBTs are then described by the second term, where $\langle \mathrm{U_c} | \mathrm{U_c} \rangle = 1$. This term is nonzero only for transitions between states having the same wave vector $\mathrm{k^i_{x,y}} = \mathrm{k^f_{x,y}}$. Furthermore, for transitions between states on different subbands (i.e., for $\mathrm{n} \neq \mathrm{n'}$) only the term proportional to e_z does not vanish. According to this polarization selection rule, ISBTs are allowed only if the electric field of the incident light has a component perpendicular to QWs. This constraint reduces the momentum matrix element describing ISBTs to

$$\langle \mathrm{f_n} | \mathrm{p_z} | \mathrm{f'_n} \rangle = \int \mathrm{dz} \varphi^*_{\mathrm{n},\mathbf{k}_{||}}(\mathrm{z}) \mathrm{p_z} \varphi_{\mathrm{n'},\mathbf{k}_{||}}(\mathrm{z}) \tag{2.10}$$

The absorption coefficient α can finally be calculated as follows [Helm, 2000]

$$\alpha_{2D} = \frac{\mathrm{n_s} e^2 \hbar}{2\mathcal{E}_0 \mathrm{cnm_c}} \mathrm{f}_{12} \frac{\Gamma}{(\mathrm{E_2}-\mathrm{E_1}-\hbar w)^2+\Gamma^2} \qquad \text{at} \quad \mathrm{k_B T} \ll \mathrm{E_F} - \mathrm{E_1} \tag{2.11}$$

where $\mathrm{n_s}$ is the density of electrons in the lowest subband per unit area and Γ is the transition linewidth. Finally, $\mathrm{f_{12}}$ is the oscillator strength given by

$$\mathrm{f}_{12} = \frac{2}{\mathrm{m_c}(\mathrm{E_2}-\mathrm{E_1})} |\langle 1 | \mathrm{p_z} | 2 \rangle|^2 = \frac{2\mathrm{m_c}(\mathrm{E_2}-\mathrm{E_1})}{\hbar^2} |\langle 1 | z | 2 \rangle|^2 \tag{2.12}$$

2.1.2 Intersubband Transitions in Valence Band

In this thesis work, I also consider the use of group-IV semiconductors (i.e., Si, Ge, and their alloy SiGe) for the development of QWIPs and ultimately Quantum Cascade Lasers (QCLs). Unlike As- and N-based materials, these group-IV semiconductors are non-polar, and therefore they are free of Reststrahlen absorption in the THz or any other spectral region. In typical Si/SiGe QWs, most of the bandgap-energy difference between the well and barrier materials falls across the valence bands. As a result holes in the valence bands can be confined more effectively than electrons in the conduction band, and therefore are better suited to the development of ISB optoelectronic devices. In order to calculate the bound-state energy eigenvalues and envelope functions of p-type Si/SiGe QWs, we have developed a self-consistent Schrodinger-Poisson equations solver based on a 6x6 Luttinger-Kohn model (Fromherz et al. 1994).

According to the **k**.**p** theory, near the center of the first Brillouin zone the valence bands [including heavy-hole (HH), light-hole (LH), and spin-orbit split-off (SO) bands] are well described by diagonalizing the 6×6 Luttinger-Kohn Hamiltonian

$$H^{0}_{\boldsymbol{\nu}'\boldsymbol{\nu}} = \begin{bmatrix} \mathrm{H_{HH}} & \mathrm{S} & -\mathrm{T} & 0 & \frac{\mathrm{i}}{2}\mathrm{S} & \mathrm{i}\sqrt{2}\mathrm{T} \\ \mathrm{S}^{*} & \mathrm{H_{LH}} & 0 & -\mathrm{T} & -\mathrm{iV} & \mathrm{i}\sqrt{\frac{3}{2}}\mathrm{S} \\ -\mathrm{T}^{*} & 0 & \mathrm{H_{LH}} & -\mathrm{S} & \mathrm{i}\sqrt{\frac{3}{2}}\mathrm{S}^{*} & -\mathrm{iV} \\ 0 & -\mathrm{T}^{*} & -\mathrm{S}^{*} & \mathrm{H_{HH}} & \mathrm{i}\sqrt{2}\mathrm{T}^{*} & -\frac{\mathrm{i}}{\sqrt{2}}\mathrm{S}^{*} \\ \frac{-\mathrm{i}}{\sqrt{2}}\mathrm{S}^{*} & \mathrm{iV} & \mathrm{i}\sqrt{\frac{3}{2}}\mathrm{S} & -\mathrm{i}\sqrt{2}\mathrm{T} & \mathrm{H_{SO}} & 0 \\ -\mathrm{i}\sqrt{2}\mathrm{T}^{*} & -\mathrm{i}\sqrt{\frac{3}{2}}\mathrm{S}^{*} & \mathrm{iV} & \frac{\mathrm{i}}{\sqrt{2}}\mathrm{S} & 0 & \mathrm{H_{SO}} \end{bmatrix} \tag{2.13}$$

where the matrix elements $\mathrm{H_{HH}}$, $\mathrm{H_{LH}}$, $\mathrm{H_{SO}}$, S, T, and V can be found in (Fromherz et al. 1994). Strain is included in this Luttinger-Kohn Hamiltonian $H^{0}_{\nu'\nu}(\mathbf{k})$ in such a way that the average energy of the three valence bands at the Γ point is constant for all values of strain. Around this constant energy value V_{av}, the three valence bands split due to strain and to the spin-orbit interaction. Thus, one can calculate the alignment of the HH, LH and SO bands at the Γ point in a QW, once the offset of the average energy (ΔV_{av}) at the heterojunction and the strain in the well and barrier layers are known.

Using the envelope function approach, the valence subband structure of any MQW system can be computed with the Hamiltonian

$$H_{\nu'\nu} = H^{0}_{\nu'\nu}\left[k_x, k_y, -i\frac{\partial}{\partial z}; z\right] + \delta_{\nu'\nu} V_{SL}(z) \tag{2.14}$$

The first term in this expression is the position-dependent Luttinger-Kohn Hamiltonian with k_z replaced by the differential operator $-i\frac{\partial}{\partial z}$. In the second term, V_{SL} is the MQW potential energy, which can be written as follows

$$V_{SL}(z) = \Delta V_{av}(z) + V_H(z) + V_{xc} \tag{2.15}$$

where the exchange correlation potential (V_{xc}), which is the many-body effects on the energy of the electron gas is given by

$$V_{xc} = -2\left[\frac{9}{4\pi^2}\right]^{\frac{1}{3}} \frac{e^2}{8\pi\varepsilon\varepsilon_0 a_0} \frac{1}{r_s}\left[1 + \frac{B}{A} r_s \ln\left[1 + \frac{A}{r_s}\right]\right] \tag{2.16}$$

A and B are equal to 21 and 0.7734, respectively. Also, $r_s = [4\pi a_0^3 p(z)/3]^{-\frac{1}{3}}$ is a dimensionless parameter characterizing the electron density, and corresponding to the mean electron distance normalized to the effective Bohr radius $a_0=(\varepsilon/m^*)/a_B$. In equation (2.15), ΔV_{av} is the position-dependent average valence-band energy at the Γ point, and the Hartree potential V_H can be calculated self-consistently using the Poisson equation

$$\nabla^2 V_H = \frac{e^2}{\varepsilon\varepsilon_0}\left[\sum \chi_i^*(\mathbf{r})\chi_i(\mathbf{r}) - N_A^-(\mathbf{r})\right] \tag{2.17}$$

where ε is the relative dielectric constant of the QW material, ε_0 is the permittivity of free space, e is the electron charge, and N_A^- is the concentration of ionized acceptors. V_H must be calculated self-consistently with the envelope functions $\chi_\nu(\mathbf{r})$, which satisfy the Schrodinger equation with the Hamiltonian of equation (2.13).

$$\sum_\nu \left[H_{\nu'\nu}\left(k_x, k_y, -i\frac{\partial}{\partial z}; z\right) - \delta_{\nu'\nu}E\right]\chi_\nu = 0 \tag{2.18}$$

To solve this equation, we introduce periodic boundary conditions and write an ansatz equation consistent with Bloch theorem:

$$\chi_\nu = e^{iqz}\sum_{k_z} c_\nu^{k_z}(k_x, k_y, q)e^{ik_z z} \tag{2.19}$$

$$k_z = \frac{2\pi}{L}n \qquad \text{and} \qquad q \in \left|-\frac{\pi}{L}, \frac{\pi}{L}\right| \tag{2.20}$$

where L is the period in the growth direction and n =0, ±1, ±2,…, . Inserting equation (2.18) into (2.19), we finally obtain a matrix eigenvalue problem for the coefficient $c_\nu^{k_z}$.

$$\sum_{\nu,k_z}\left[H_{\nu'\nu}^{k_z'k_z}(k_x, k_y; q) - \delta_{\nu'\nu}\delta_{k_z'k_z}E\right]c_\nu^{k_z} = 0 \tag{2.21}$$

where

$$H_{\nu'\nu}^{k_z'k_z}(k_x, k_y; q) = \int_0^{L_z}\frac{dz}{L_z}e^{-i(q+k_z')z}H_{\nu'\nu}(k_x, k_y, -i\frac{d}{dz}; z)e^{i(q+k_z)z} \tag{2.22}$$

2.2 Quantum Well Infrared Detectors (QWIPs)

QWIP operation is based on the photoemission of electrons or holes from QWs. Therefore, the QWIP active region is engineered in such a way that carriers can be excited from the QW ground state to the first excited state by photon absorption, and then scattered into the continuum of unbound states over the barriers, where they create a photocurrent under an externally applied electric field. Efficient escape from the QWs requires that the first excited state is in resonance with the barrier energy (bound to quasi-bound QWIP) (B. F. Levine 1993; H. C. Liu 1993). The resulting photocurrent is measured at the device electrical contacts.

2.3 Basic Operation

All QWIP structures are designed in such a way that the energy separation between the two lowest bound states of the QWs E_2-E_1 matches the energy $\hbar\omega$ of the infrared photons to be detected. This is accomplished by changing the well width to tune the energies of the ground state (E_1) and 1st excited state (E_2). Also, the choice of alloy composition determines the position of the 1st excited state relative to the barriers. Depending on this relative position, different QWIP configurations can be distinguished, named bound-to-bound (E_2 well below the barrier), bound-to-quasi- bound (E_2 in resonance with barrier) and bound-to-continuum (E_2 above the barrier), as shown in Figure 2.3 (H.C. Liu 2000). The first bound-to-bound QWIP device was demonstrated by Levine et al.(Levine et al. 1987).

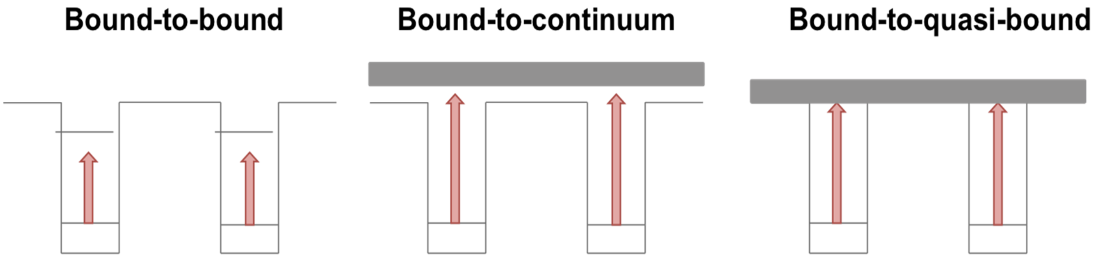

Figure 2.2 Schematic energy band diagram of the three different types of QWIPs

In the bound-to-continuum case, an electron (or hole) in the ground state is directly photo-excited out of the QW into the continuum of unbound states over the barriers. This can be realized by decreasing the width of the well layer, so that the first excited bound state can be pushed up into the continuum. This QW structure has the major advantage that the photo-excited carriers can escape from the QWs with essentially 100% probability, due to the unconfined nature of the final states of the ISBTs. However, the oscillator strength (and therefore the absorption probability) is not as large as in bound-to-bound QWIPs, due to the smaller spatial overlap between the initial and final states. On the other hand, bound-to-bound QWIPs suffer from a reduced escape probability. Finally, in the bound-to-quasi-bound case the 1st excited state is in resonance with the top of the barrier. Of the three designs, the bound-to-quasi-bound QWIP has the best performance as it gives the best compromise between absorption strength and escape probability.

2.4 Key Parameters

The optimization of a detector design takes into account some key parameters, such as photoconductive gain, responsivity, detectivity, blip temperature, and quantum efficiency. In practice, the dark current that flows in the absence of incident light often limits the detector performance.

2.4.1 Responsivity (R)

The responsivity of a photoconductor is the magnitude of the photocurrent signal per unit optical power (units: A/W). In a QWIP, the responsivity R can be written in terms of the photoconductive gain g_p and quantum efficiency η as follows

$$\mathrm{R} = \frac{\mathrm{q}}{\mathrm{h}\omega}\eta \mathrm{g_p} \tag{2.23}$$

$$\mathrm{g_p} = \mathrm{P_e}\frac{1}{\mathrm{P_c}}\frac{1}{\mathrm{N_{QW}}} \tag{2.24}$$

$$\eta = 1 - \mathrm{e}^{-\alpha \mathrm{N_{QW}}} \tag{2.25}$$

where p_e is the escape probability from the QW into the continuum above the barrier for a photoexcited electron, p_c is the capture probability of an electron from the continuum into the QW, N_{QW} is the total number of QWs in the active region, and α is the absorption coefficient (it is dimensionless). The quantum efficiency is proportional to N_{QW} and α when $\alpha N_{QW} << 1$,i.e.,

$$\eta = 1 - \mathrm{e}^{-\alpha \mathrm{N_{QW}}} \cong 1 - (1 - \alpha \mathrm{N_{QW}}) \approx \alpha \mathrm{N_{QW}} \tag{2.26}$$

Therefore, in this regime the responsivity is constant with the number of wells N_{QW}. Furthermore, since the absorption coefficient is proportional to the doping density N_D, the responsivity increases with increasing doping density in the regime where $\alpha N_{QW} << 1$. When $\alpha N_{QW} >> 1$, the quantum efficiency goes to unity and the responsivity becomes inversely proportional to the number of wells but constant with doping.

2.4.2 Detectivity (D) and Blip Temperature (TBLIP)*

The detectivity (D*) and blip (background limited IR performance) temperature (T_{BLIP}) are the two most important characteristics of an infrared detector. The detectivity D^* is the signal (per unit incident power) to noise ratio normalized by the detector area A and the measurement electrical bandwidth Δf, i.e.,

$$D^* = \frac{R_p}{i_n}\sqrt{A\Delta f} \tag{2.27}$$

where R_p is the peak responsivity in A/W and i_n is the root mean square noise current. The units of D^* are Jones [J], which correspond to $\mathrm{cm}\sqrt{\mathrm{Hz}}/\mathrm{W}$. The noise contribution can come from the detector itself (dark current) and from fluctuations of the photocurrent induced by background photons incident on the detector. The BLIP temperature T_{BLIP} is the characteristic temperature at which the background photocurrent equals the dark current.

The detector-noise-limited detectivity is given by

$$D^* = \frac{\lambda}{2hc}\frac{\eta}{\sqrt{N_{QW}}}\sqrt{\frac{\tau_{life}}{N_{2D}}} \tag{2.28}$$

$$N_{2D} = \frac{m}{\pi\hbar^2} k_B T \ln[1 + e^{\frac{E_f}{k_B T}}] \tag{2.29}$$

where τ_{life} is the capture lifetime which is typically short in QWIPs. Based on equations (2.27) and (2.28), we conclude that in the regime where $\alpha N_{QW} << 1$ the detector-noise-limited D* increases with the square root of the N_{QW} and of N_{2D}. Viceversa, D* becomes inversely proportional to $\sqrt{N_{QW} N_{2D}}$ when $\alpha N_{QW} >> 1$.

In the blip regime (i.e., for $T < T_{BLIP}$), the dominant noise is caused by the background photons and it is desirable to operate the detector under this condition. The background limited D* is given by

$$D^*_{BLIP} = \frac{\lambda}{2hc}\sqrt{\frac{\eta}{\phi_{B,ph}}} \tag{2.30}$$

where $\phi_{B,ph}$ is the integrated background photon flux incident on the detector. It is seen from the equation (2.30) that D* depends only on the quantum efficiency and the background photon flux. In order to find T_{BLIP} one needs to solve the following transcendental equation (Hao et al. 2014).

$$\eta^{(1)} \tau_{life} \phi_{B,ph} = 2L_p (\frac{m_b^* k_B T}{2\pi\hbar^2})^{3/2} \exp(\frac{E_F}{k_B T} + \frac{hc}{\lambda k_B T}) \tag{2.31}$$

Noting that $\eta^{(1)} \propto N_D \propto E_f$, we find the T_{BLIP} is maximized for $Ef = 1.37k_BT$. More details of this calculation can be found in (Hao et al. 2014).

3 C-PLANE NITRIDE THz QUANTUM WELL INFRARED PHOTODETECTORS (QWIPs)

3.1 Motivations

THz device technologies play a key role in many important military and civilian applications, such as security screening, industrial quality control, and spectroscopic imaging. State-of-the-art THz semiconductor devices, including photodetectors (Baumann et al. 2005; Vardi et al. 2008)., and quantum cascade lasers (G Scalari et al. 2006; Walther et al. 2007; Giacomo Scalari et al. 2003; Faist et al. 1994), are currently based on ISBTs in arsenide-based QWs. However, these devices still suffer from key limitations. Most notably, GaAs-based materials exhibit lattice vibrational modes or phonons that couple to light in the THz region. In particular, the coupling of photons with longitudinal optical (LO) and transverse optical (TO) phonons in polar crystals creates a frequency band, called the Reststrahlen band, where light propagation is completely prohibited as shown in Figure 3.1. In GaAs/AlGaAs QWs, the Reststrahlen band lies in the range of about 8 - 9 THz, rendering this materials system useless for the development of optoelectronic devices near this frequency range. The second fundamental limitation of GaAs-based materials for THz ISB device applications is poor performance at high temperatures.

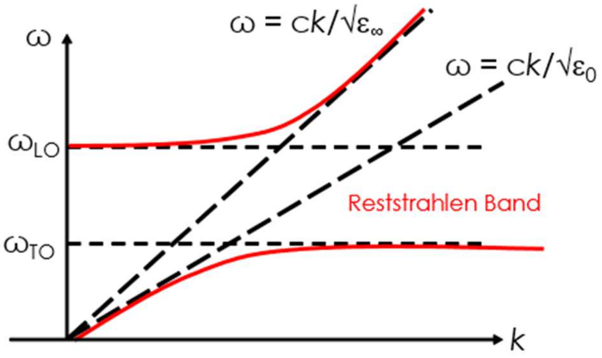

Figure 3.1 Dispersion relation of coupled phonon-photon modes in polar crystal. Light propagation within the Reststrahlen band is strictly prohibited since the material is strongly absorbing and only decaying waves are supported.

Recently it has been argued that these limitations can be overcome using GaN/AlGaN QWs (Bellotti et al. 2008; Sushil et al. 2009). Since the Reststrahlen band of GaN-based materials lies between 16 - 22 THz, GaN/AlGaN QWs can be used as the material of choice for the entire THz spectral range (0.3 - 10 THz). In addition, because the LO-phonon energy of GaN is almost three times higher than that of GaAs, GaN-based THz ISB devices (particularly sources) are expected to have a higher maximum operating temperature than their GaAs counterparts.

So far the investigation of ISBTs in III-nitride materials has mostly focused on the near-infrared and fiber-optic communication spectral regions. Several III-nitride optoelectronic devices, including electro-optic modulators, light emitters, and photodetectors, have been reported at near-infrared wavelengths (Suzuki and Lizuka 1998; Hofstetter et al. 2008; Hofstetter et al. 2003; Iizuka, Kaneko, and Suzuki 2006; Li et al. 2007; F. Sudradjat et al. 2010). The development of similar devices operating at THz and more in general far-infrared (FIR) wavelengths is particularly complicated by the large internal electric fields due to spontaneous and piezoelectric polarizations in III-nitride QWs. In addition, the material quality of the required MQW structures is limited by the large lattice and thermal mismatch of these QWs with the foreign substrates that are commonly used in their growth.

3.2 Methods

In this section I will discuss the experimental methods, which involve the active-region growth, fabrication, and characterization of the ISB devices of interest. First, I will give a brief summary of the growth methodologies. Then, I will present a high-yield and reproducible device fabrication process in detail. Finally, I will discuss the electrical and optical characterization methods.

3.2.1 Device growth and fabrication

The active material of the initial III-nitride QWIPs developed in this work was grown by Wei Zhang in Boston University's Wide Bandgap Semiconductor Laboratory (WBSL) using plasma-assisted MBE. The WBSL MBE reactor has Ga, Al, Si, In, and Mg effusion cells with an adjustable electronic temperature control unit. The reactive nitrogen is provided through the use of a radio frequency (RF) plasma. A Si cell is used for n-type doping after calibration of the electron density via Hall effect measurements. The growth conditions are monitored in real time via reflective high-energy electron diffraction (RHEED).

Initially the substrate is degreased using perchloroethylene, acetone, methanol, isopropanol, and water, and then blow-dried with nitrogen gas. Next, the substrate is loaded into the MBE chamber for several hours of dehydration bake at 500 ˚C to remove any trace of water. The desired epitaxial film is then grown under Ga rich condition in high vacuum ($<10^{-9}$ torr). The sample growth starts with an n-doped template layer whose thickness is around 300 nm. The temperature is carefully varied between 700 ˚ and 750 ˚C to make sure that the growth mode is two-dimensional, in which case bright and streaky RHEED patterns are observed. Then, the MQW active region is grown epitaxially at a 1 Å/s growth rate via automatic control of the effusion cells with a custom-made Labview software. The growth is completed with a 200-nm-thick n-doped cap layer. The sample surface is then studied by atomic force microscopy (AFM) and scanning electron microscopy (SEM). In addition, in order to determine the QW periodicity and average Al composition, X-ray diffraction (XRD) analysis is used. Based on the XRD data, one can determine the actual growth results to be used in simulations to model the device performance.

After sample growth, mesa structures (with $450x400\mu m^2$ area) are fabricated using photolithography and Reactive Ion Etching (RIE). Metal contacts consisting of a Ti/Al/Ti/Au multilayer structure are then deposited on top of and around each mesa. After annealing at 850 ᵒC for 50 s, values on the order of 10^{-4} $\Omega\text{-cm}^2$ are measured for the contact resistivities. Forming gas annealing is also performed in order to passivate defects on the mesa sidewalls, which might cause leakage current paths. Since only the electric field component perpendicular to the QW layers (i.e., TM-polarized light) interacts with

ISBTs, the sample geometry must ensure that this condition is satisfied. To this purpose, the sample can be illuminated at an oblique angle (usually the Brewster angle); alternatively, a 45^{o} multipass waveguide geometry or a grating coupler can be used (Arslan, Colakoglu, and Besikci 2013; Sarusi et al. 1994; R. Zhang et al. 2011). In this work, we used suitable gratings patterned in the top metal contacts to diffractively scatter the input light, since the GaN growth substrate is opaque at FIR wavelengths due to its relatively high background n-doping, which make it impossible to couple the light through an angled facet. For optimal coupling, the periodicity of the grating should be approximately equal to the wavelength of the incident light inside the material. Once the ohmic contacts and metallic gratings have been fabricated, another metallization step is performed to create bonding pads, consisting of a Ni (30 nm)/Au (250 nm) film. Finally, the devices are wire-bonded with a gold ball bonder to two external gold pads. A schematic side view and an optical micrograph of a fully mounted device are shown in Figure 3.2.

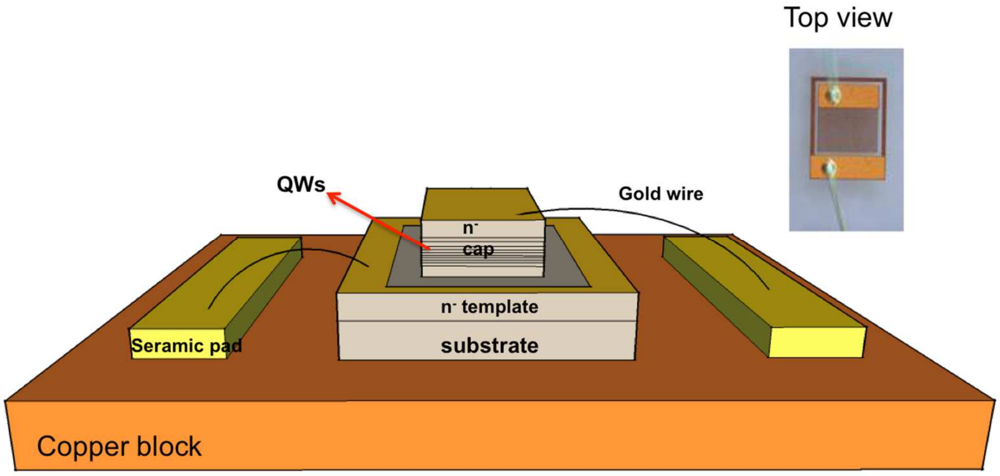

Figure 3.2 Schematic side view and top-view optical image of mesa device

3.2.2 Photolithography

Photolithography is the process of transferring geometrical patterns from a glass mask to the surface of a semiconductor substrate. This method is very common for processing device mesas, metal contacts, bonding pads, etc., in academia and industry. There are two types of photolithography implemented in this work. One is positive-tone lithography, where the areas of the photoresist that are exposed to the UV light are dissolved, while the other regions remain on the sample as a coating. Positive-tone photolithography has a high degree of reproducibility and is easy to use; however, it is not suitable for the fabrication of the gratings in the top metal contacts, which involve very narrow features (a few μm). The absorption of UV light by a photoresist decreases with increasing depth into the photoresist. As a result, the top part of the photoresist is exposed to the morelight than the bottom part. This behavior yields a positive slope in the photoresist sidewall, which causes poor lift-off. To overcome this issue in the grating fabrication, I use negative-tone photolithography where the areas of the photoresist that are exposed to the UV light remain on the sample, while the rest is dissolved during the development process. In my all device fabrication, I used AZ 5214 E positive-tone photoresist, manufactured by Clariant.

The steps involved in positive-tone photolithography are: sample cleaning, photoresist application, soft baking, mask alignment, exposure and development, as described in more detail in the following:

1) Initially degrease and sonicate the sample in acetone (acetone can be heated up to 50 ˚C if needed for dirty substrates). Then clean it using acetone, methanol,

isopropanol, and water, and blow-dry the surface with nitrogen gas to remove any particulate matter, as well as any traces of organic/ionic impurities.

2) Wash the sample in isopropanol and methanol, and rinse it in distilled water.
3) Blow dry with nitrogen and pre-bake on a hot plate at 105 ˚C for one minute to evaporate any trace residue of water.
4) Spin-coat the surface with photoresist in a Headway spinner, as shown in Figure 3.3(b).
    a) Place the substrate on the vacuum chuck of the Headway spinner
    b) Gently shake the AZ 5214 E photoresist to ensure that the solution is well mixed. Use a pipette to drop some photoresist on the surface without transferring any bubble.
    c) Spin the substrate at a speed of 2000 rpm, with a 20000 rpm/sec ramp in 45 sec. The photoresist thickness obtained with this recipe is about 2 µm, which is large enough to produce an adequate mask for the mesa etching.
5) Remove the sample from the spinner and bake it for one min at 110 ˚C on a hot plate.
6) If the substrate size is too small to place in the mask aligner (Karl-Suss MA6), it can be bonded on a Si wafer using the same photoresist as glue.
7) Place the wafer on the mask aligner chuck, align the mask plate to the sample with a 50-µm gap, and expose the sample for 12 sec in vacuum. Set the light source to channel-1 at 10 mW/cm^2 intensity.

8) Develop the sample in 4:1 diluted (with water) alkaline-based AZ 400 K developer for about 15 sec. Then rinse the sample under running water for at least 30 sec. Resulting mesa structure is shown in Figure 3.3(c).
9) Blow-dry the sample with nitrogen gas and check the lithographic features patterned in the photoresist under a microscope.
10) Use a plasma asher with 300-W power and 150 standard cubic centimeter per minute (sccm) gas flow for 1-2 mins to remove any possible microscopic photoresist residue.

The negative-tone lithography recipe that I used for the gratings and metal contacts is described in the following:

1) The AZ 5214 E photoresist is used with an additional step to achieve the image reversal effect. The same steps 1-6 as in the positive-tone procedure above are followed, except for different spinner parameters (4000 rpm spin speed, 1000 rpm/sec ramp, 45 sec spin time).
2) Place the wafer on the mask aligner chuck and set the exposure parameters as follows: 50-µm gap, 4-sec exposure time, 10-mWatt/cm^2 light intensity, and vacuum mode for minimizing the UV light diffraction.
3) Bake the sample on a hot plate at 120 ˚C for 2 minutes together with the Si wafer.
4) Then place the sample back in the mask aligner for flood exposure for one minute using 10-mWatt/cm^2 light intensity. During flood exposure, the photolithography mask is removed so that the whole sample surface is exposed to the UV light continuously for 60 sec. The areas that were initially exposed to the UV light are

exposed again, and as a result become insoluble. Vice versa, the other areas still retain the properties of positive-tone photoresist. A fabricated mesa structure covered with photoresist after the second photolithography step is shown schematically in Figure 3.3(f) and (i).

5) Follow steps 8-10 as in the positive-tone procedure. This recipe gives reproducible results for feature size as small as 3 µm with a photoresist thickness of 1.5 µm.

3.2.3 RF- Reactive ion etching

QWIPs require bottom and top contacts where the carriers are injected and collected. The bottom contact layer is buried under the MQW active region and therefore needs to be exposed before an ohmic metal contact can be deposited. For that purpose, Reactive Ion-Etching (RIE) is used to fabricate rectangular mesas etched through the MQWs into the bottom contact layer as shown in Figure 3.3(d). The RIE recipe that I use is as follows. The RIE chamber is cleaned with 10-sccm O_2 flow under 250-W plasma power for 15 minutes in a 50-mTorr chamber pressure. The chamber is then further cleaned with 50 sccm of Cl_2 and Ar (at a flow rate of 4 and 46 sccm, respectively) with a power of 100 W for an hour under 50-mTorr chamber pressure. Next, a dummy conditioning process is run to set the environment ready for the actual etching. Specifically, Cl_2 and Ar with 20 and 6 sccm gas flow rates are used to create a plasma with a power of 175 W in a 15-mTorr chamber pressure for 7 minutes and 30 seconds. This conditioning process is run at time intervals of 3 minutes run and pause, 3 minutes run and pause, and 2 minutes run and stop, to prevent overheating of the system. After conditioning, a similar GaN/AlGaN MQW sample with the same Al composition is used for calibration with the same recipe as for conditioning. Based on the etch rate obtained with this sample, the time required for the target etch depth is determined. Finally, the actual sample is etched using the same recipe. With this procedure, the targeted etch depth can be achieved quite precisely.

3.2.4 Metallization

As I discussed earlier in section 2.1, the ISB polarization selection rules require that only light polarized parallel to the growth direction can be absorbed or emitted. In this work, I used one-dimensional metallic gratings to diffract a normally incident beam of light leading to in-plane propagation inside the semiconductor, as often used for ISB photodetection applications (Liu, Capasso). The periodicity of the grating needs to be approximately equal to the wavelength of the absorbed light inside the material for optimum coupling.

GaN/AlGaN QWIPs require n-type contacts for both the top and bottom electrodes, since their operation only involves one type of carriers (electrons). In this work, I used Ti/Al/Ti/Au ohmic contacts, which are well established for n-doped GaN materials (Motayed et al. 2003) (Kim, Jang, and Lee 2002). To fabricate these contacts, negative photolithography is used following the recipe of section 3.2.2 to transfer the grating patterns on the top electrode, as shown in Figure 3.3(f) and (g). Next, the contact is annealed under nitrogen ambient condition at 850 ˚C, so that a TiN alloy forms at the Ti-GaN interface (Ruvimov, Liliental-Weber, and Washburn 1996). This TiN film forms a thin depletion region at the metal-semiconductor junction for suitable electron tunneling. The use of Al allows for better current injection, since the Al work function almost matches the electron affinity of GaN (Foresi and Moustakas 1993). The final Ti/Au bilayer is there to protect Al from being oxidized and also helps improving the subsequent wire bonding.

After the negative-tone photolithography step, the sample surface is treated with a plasma asher, followed by a bath in a H_2O:HCl (1:1) acidic solution for 60 seconds to remove any native oxide layer introduced during plasma ashing. Immediately after this acid treatment, the sample is loaded in an electron-beam evaporator (CHA), and the Ti (10 nm) / Al (120 nm) / Ti (40 nm) / Au (80 nm) multilayer film is deposited. Finally, a lift-off process with acetone followed by a water rinse is applied to remove the unwanted metal regions with the photoresist mask. An additional metallization step, also based on negative-tone photolithography, is finally employed to pattern bonding pads consisting of a Ni (30 nm) / Au (250 nm) bilayer, as shown in Figure 3.3(i) and (j). An optical micrograph of a completed device is shown in Figure 3.2.

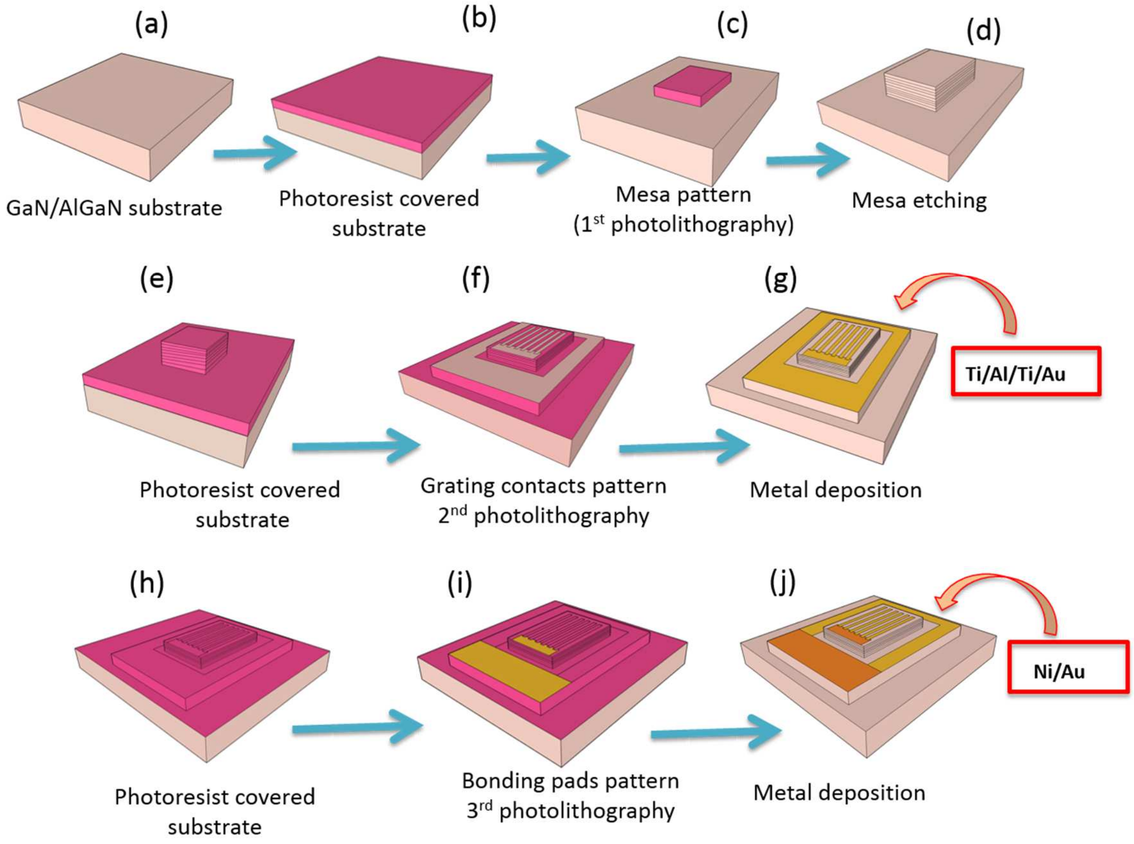

Figure 3.3 Fabrication flow of the QWIP device

3.3 Electrical characterization

For electrical characterization, the device shown in Figure 3.2 is mounted on the cold finger of a continuous-flow liquid-helium cryostat to carry out the measurements at different temperatures. The sample temperature is controlled electronically with a LakeShore 321 Auto-tuning Temperature Controller. To measure the IV characteristics of the device, the sample is mounted in the cryostat and pumped to the pressure level of ~ 10^{-5}-10^{-6} torr prior to being cooled with either liquid Nitrogen or liquid Helium.

We have developed a Matlab program that controls a Hewlett Packard 8114A high-power pulse generator and a Tektronix TDS 2024 oscilloscope through the IEEE-48 standard General Purpose Interface Bus (GPIB) to supply voltage to the device and measure the current with a transformer. This program automatically stores all the data. The circuit schematic of the IV measurement setup is shown in Figure 3.4.

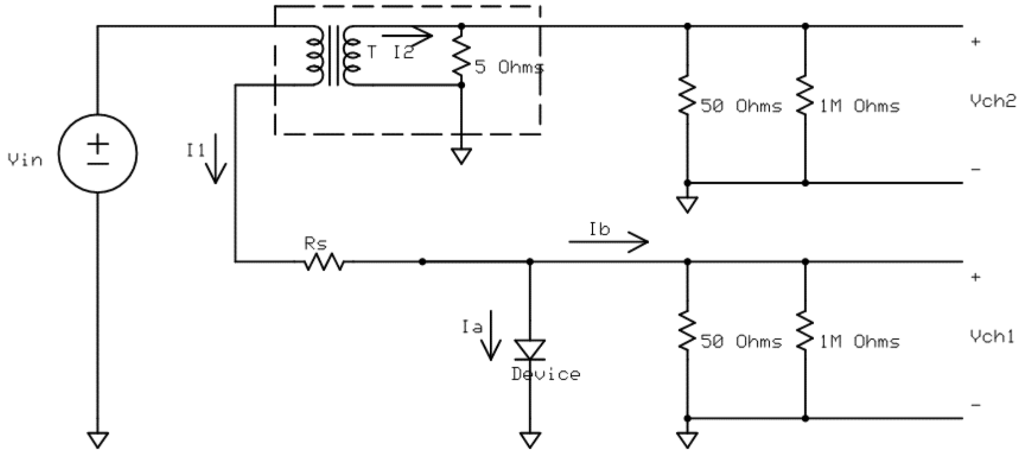

Figure 3.4 Schematic diagram of the circuit used for the IV measurements. Vin represents the HP 8114A voltage source and the device is shown symbolically as a diode. Vch1 and Vch2 are the input channels 1 and 2 of the Tektronix oscilloscope. The current-to-voltage transformer is shown by the dashed rectangle

Using this circuit we can determine the voltage across (V_{ch1}) and the current through (I_a) the device from the oscilloscope channels Ch1 and Ch2, respectively. Each channel has an input impedance of 1 MΩ, and is connected to a 50-Ω shunt resistor for impedance matching. The current through the device can be calculated as a function of the voltages measured at the input channels of the oscilloscope. From the turn ratio of the transformer N_1/N_2 we have:

$$\frac{N_1}{N_2} = \frac{1}{20} = \frac{I_2}{I_1} \rightarrow I_1 = 20I_2 \tag{3.1}$$

I_2 can be written using Kirchhoff’s current law as follows

$$I_2 = \frac{V_{ch2}}{\left[\frac{1}{5} + \frac{1}{50} + \frac{1}{10^6}\right]^{-1}} = \frac{V_{ch2}}{4.5454} \tag{3.2}$$

The total current produced by the source V_{in} is

$$\mathrm{I_1 = I_a + I_b} \tag{3.3}$$

where I_a is the current through the device and

$$\mathrm{I_b} = \frac{\mathrm{V_{ch1}}}{\left[\frac{1}{50} + \frac{1}{10^6}\right]^{-1}} = \frac{\mathrm{V_{ch1}}}{50} \tag{3.4}$$

Combining equations (3.1), (3.2), (3.3), and (3.4) we obtain the current through the device as follows:

$$\mathrm{I_a = A.\,V_{ch2}} - \frac{\mathrm{V_{ch1}}}{\mathrm{B}} \tag{3.5}$$

where the constants A and B are equal to 4.4 and 50, respectively. In practice these constants can be determined experimentally by measuring the IV characteristics of a calibrated resistor.

3.4 Optical characterization (Photocurrent Measurement)

The device photocurrent spectra were measured using a Bruker Vertex 70V Fourier transform infrared spectrometer (FTIR) equipped with a globar source and Mylar beamsplitter, via step-scan phase modulation and lock-in detection. In the phase-modulation mode, the moving mirror of the interferometer is jittered sinusoidally in time with a frequency of 1.3 kHz and amplitude of 1 μm at each step, to create a modulated optical beam propagating through the interferometer. More details about phase modulation can be found in (J. Chamberlain 1971; J. Chamberlain and Gebbie 1971).

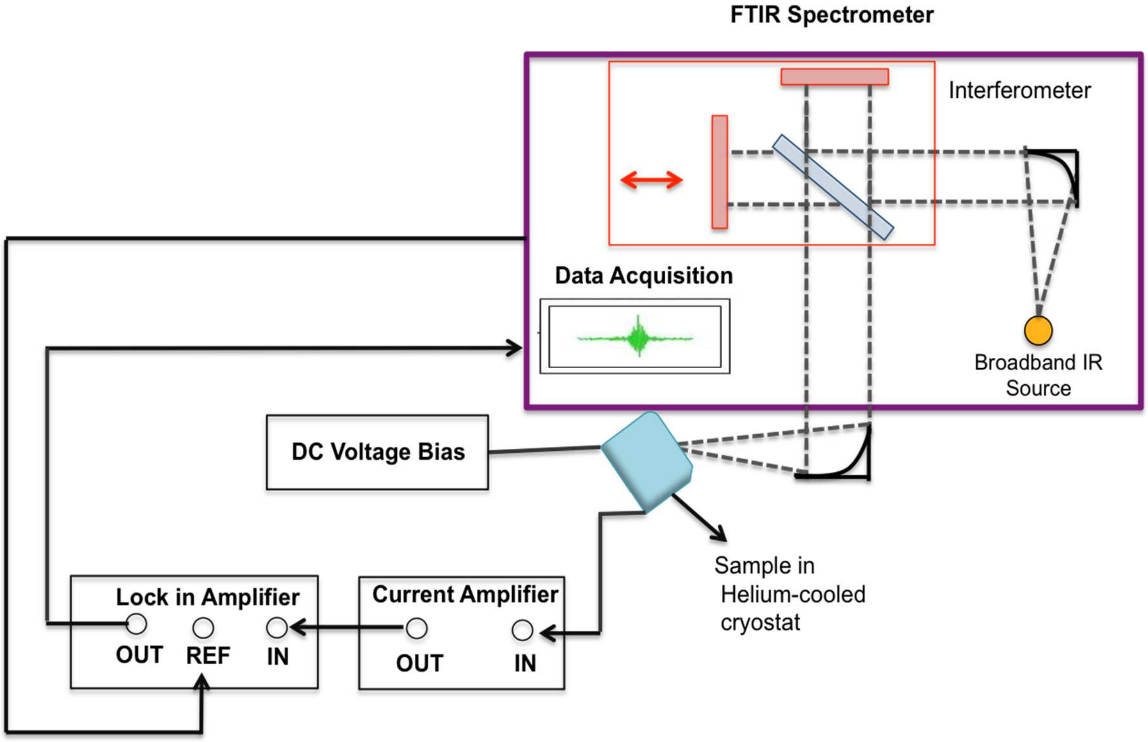

Figure 3.5 Photodetection experimental set up

The experimental setup used in these measurements is shown in Figure 3.5. The sample is mounted on the cold finger of a continuous-flow liquid-helium cryostat and placed in front of the exit port of the FTIR as an external detector. The phase-modulated infrared light from the FTIR is focused onto the detector with a parabolic mirror (with an f-number of 1.25) and detected via step-scan phase modulation. The detector is biased with an Agilent DC voltage source. The DC bias and modulated AC signal from the detector are decoupled with a bias-T where a capacitor is used to filter out the DC component. The AC output from the bias-T is then fed into a Stanford Research SR570 transimpedence amplifier followed by an SR530 lock-in amplifier, which is synchronized to the modulation frequency of the FTIR mirror. Finally, the output of the lock-in amplifier is fed back into the FTIR for data analysis.

3.5 Initial THz QWIP Results

In our initial work (F. F. Sudradjat et al. 2012), we have demonstrated photodetectors based on ISBTs in GaN/AlGaN double-step QWs with responsivity peaked at a photon energy of about 54 meV (13 THz, 23 µm). To introduce and motivate the double-step design, in Figure 3.6 (a) the conduction-band lineup and squared envelope functions of a GaN/AlGaN multiple QW structure under bias are shown, as computed using our Schrodinger equation solver including the internal electric fields. The ISB absorption energy between the ground state and the first excited state is about 50 meV (i.e., in the FIR range of interest in this work). In order to get such small transition energy, a large well width (57 monolayer (ML), 1ML=2.6 Å) is used, which causes both ground state and first excited state to fall within the triangular portion of the QW. As a result, even though barriers with very small Al content (8 %) are used, the first-excited sub-bands necessarily remain well below the top of the barriers, which limits the escape efficiency.

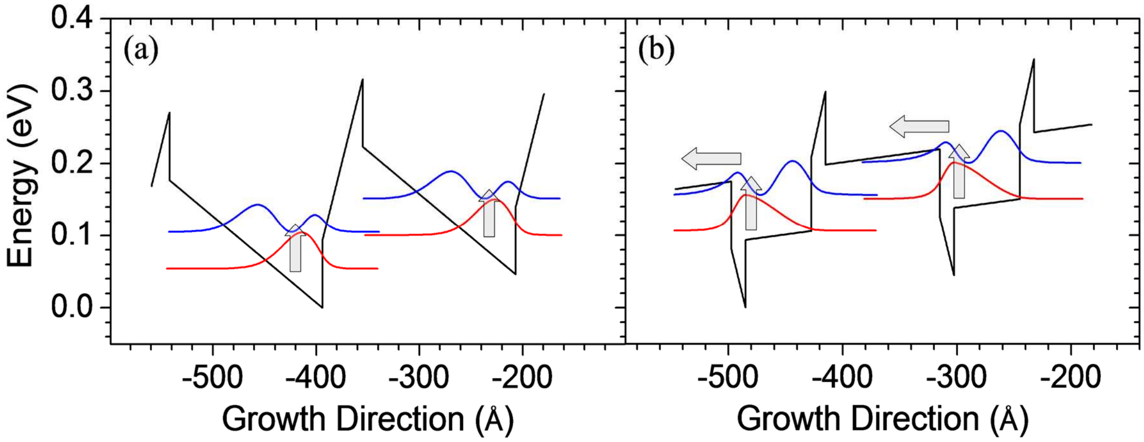

Figure 3.6 Conduction-band lineups and squared envelope functions of the relevant bound states of two FIR QWIPs under bias, where each repeat unit consists of: (a) a single Al0.08Ga0.92N barrier and a single GaN well; (b) a step Al0.16Ga0.84N/Al0.08Ga0.92N barrier and a step GaN/Al0.08Ga0.92N well. The vertical and horizontal arrows indicate, respectively, photon absorption and photoelectron escape.

By using a double-step QW design, a nearly rectangular potential energy profile can be obtained as shown in Figure 3.6(b). In particular, in order to effectively eliminate the large internal electric fields, we use two different (Al)GaN compositions both in the wells and in the barriers. Therefore, bound-to-quasi-bound QWIP structures can be designed for optimal photon absorption and carrier escape, similar to As-based devices. The ISBT energy of the device of Figure 3.6(b) is computed to be 49 meV. In this structure, each step well consists of 5 MLs of GaN and 22 MLs of $Al_{0.08}Ga_{0.92}N$, while 5 MLs of $Al_{0.16}Ga_{0.84}N$ and 38 MLs of $Al_{0.08}Ga_{0.92}N$ are used in each step barrier. For optimal performance (bound-to-quasi-bound case) the first-excited subbands are well confined within the QWs, while at the same time being energetically close to the overlaying continuum.

Twenty repetitions of this double-step QW structure (beginning and ending with the 38-ML-thick $Al_{0.08}Ga_{0.92}N$ barrier layer) were grown on a 1 x 1 cm^2 substrate of commercially available free-standing GaN using rf plasma-assisted MBE. The active region is embedded between a GaN template layer and a 200-nm-thick $Al_{0.08}Ga_{0.92}N$ cap layer, both of which are n-doped with Si to the level of 1×10^{18} cm^{-}3. The composition of the cap layer is chosen as to eliminate the band bending due to intrinsic electric fields, as confirmed with simulations based on the NextNano3 software. The 5-ML-thick GaN layer in each well is n-doped at $6x10^{18}cm^{-3}$ in order to obtain strong ISB absorption. X-ray diffraction data shows superlattice satellite peaks from which one can infer the repeat-unit thickness and average composition.

The dark current-voltage (I-V) characteristics of a device based on the design of Figure 3.6(b), measured under forward and reverse bias at different heat-sink temperatures, are shown in Figure 3.7. A nearly linear I-V behavior is observed at 100 K and above, indicating efficient thermal escape of electrons from the QWs. As the temperature is decreased, more and more electrons in the well occupy states near the bottom of the ground-state subbands, and as a result the current becomes dominated by tunneling, leading to a pronounced turn-on in the I-V curves.

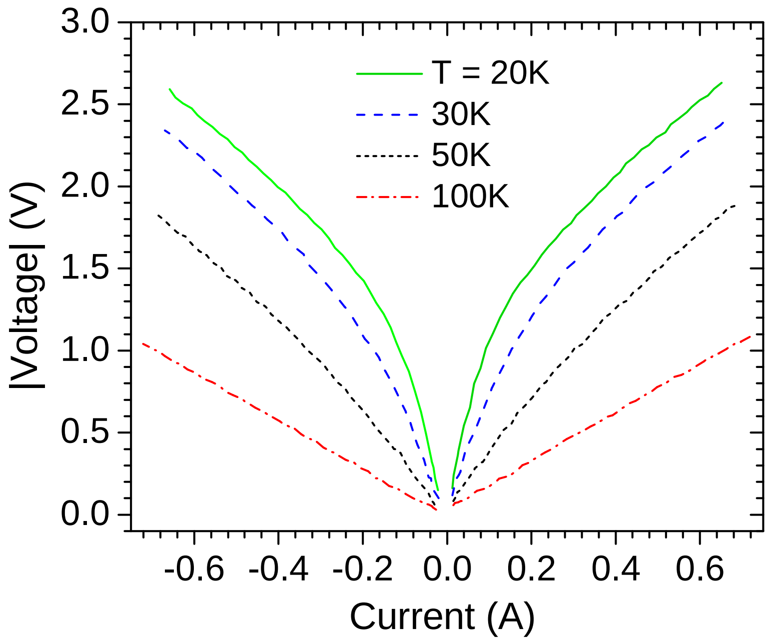

Figure 3.7 Temperature dependent IV characteristics of a device based on the design of Figure 3.6(b).

The total photocurrent signal of a device with 9-μm grating period measured at 20 K is plotted as a function of applied DC bias in Figure 3.8(a). As the voltage is increased in either forward or reverse direction, the first excited state of each QW becomes more and more strongly coupled to the adjacent barrier continuum, leading to an increase in photoelectron extraction efficiency and therefore in photocurrent. At the same time, the oscillator strength of the absorbing transitions decreases due to the reduced confinement of the upper states, and as a result the photocurrent eventually saturates as the bias voltage is further increased. Also, the photocurrent signal decreases with increasing device temperature, due to increased thermal escape from the QWs, until it can no longer be resolved above the noise floor at about 50 K (where the I-V characteristics also become predominantly linear).

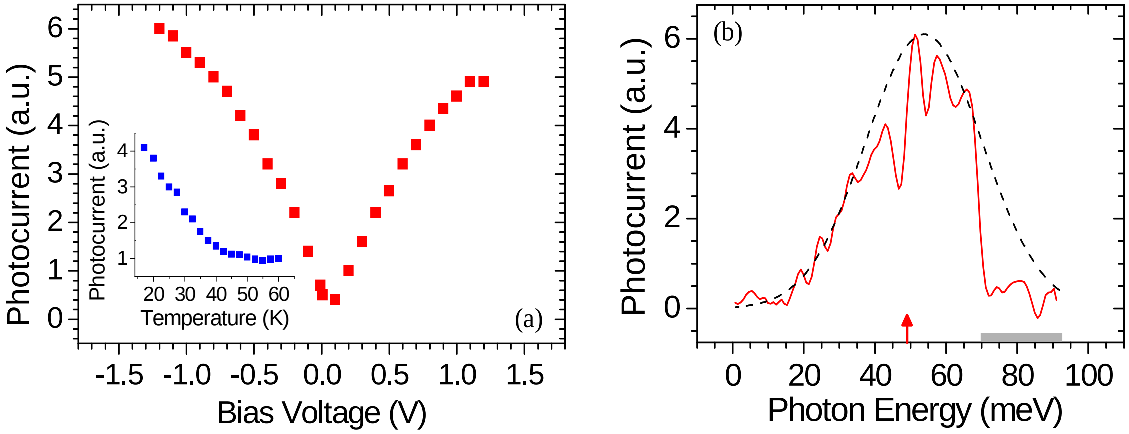

Figure 3.8 (a) Photocurrent signal of a double-step AlGaN FIR QWIP at 20 K versus applied voltage. Inset: photocurrent of the same device versus temperature. (b) Photocurrent spectrum of the same device (solid line), and Gaussian fit (dashed line). The grey band near the horizontal axis indicates the Reststrahlen band of GaN. The vertical arrow indicates the calculated transition energy.

The photocurrent spectrum of the same device at 20 K is shown in Figure 3.8(b) (solid line). The sharp cutoff on the short-wavelength side is due to the onset of the Reststrahlen band of GaN, while the dips observed near the peak are caused by atmospheric absorption. The dashed line shows a Gaussian fit to the measured data. The photon energy of peak responsivity at (54 meV) is in close agreement with the calculated value (49 meV). The device responsivity was measured by comparing these data with those obtained with a calibrated pyro-electric detector. A peak value around 7 mA/W was found, which is comparable with the responsivity of the GaAs THz QWIPs demonstrated so far operating at longer wavelength (Graf et al. 2004a; Luo et al. 2005; A.G.U. Perera et al. 2000; Patrashin and Hosako 2008a).

4 SEMI-POLAR NITRIDE THz QUANTUM WELL INFRARED PHOTODETECTORS (QWIPs)

4.1 Motivations

As I discussed previously, typical III-Nitride QWs grown along the polar crystallographic *c* axis contain strong internal electric fields due to spontaneous and piezoelectric polarizations. These internal fields produce a trapezoidal conduction- and valence-band lineup that tends to blue-shift the ISB transition energies, and therefore can significantly complicate the development of long-wavelength ISB devices. In addition, in QWs designed for THz-range ISB transitions, the first-excited states necessarily fall within the triangular portion of the band lineup, well below the top of the barriers, as clearly shown in Figure 3.6(a). As a result, carrier extraction from these subbands into the overlaying continuum of unbound states (as needed for efficient ISB photodetection) becomes extremely difficult. For the same reason, interwell tunneling transport (which forms the basis of quantum cascade laser operation) is equally problematic among the lower-energy states of these QWs. By designing double-step QWs, these effects can be reduced as shown by the simulation and experimental results of the previous section. However, a potential drawback of these structures is the increased interface roughness scattering due to the presence of additional hetero-interfaces in each QW period.

An alternative approach to address the same design challenge is the use of QWs grown along semi-polar (or nonpolar) crystallographic directions, where the undesirable internal electric fields are significantly reduced (or completely eliminated). The growth of III-nitride semiconductors along such directions is the subject of strong research interest for both fundamental and technological reasons, (J. S. Speck and S. F. Chichibu 2009) and has greatly benefited in recent years from the commercialization of high-quality semi-polar and nonpolar free-standing GaN substrates. Nonpolar *m*-plane III-nitride QWs have already been used for the measurement of THz ISB absorption, (C B Lim et al. 2015; Edmunds et al. 2014), as well as the investigation of mid-infrared ISB transitions (C. B. Lim et al. 2015; Kotani, Arita, and Arakawa 2014). In the following sections, I will give background information and discuss device design, fabrication, and characterization.

4.2 Background Information

III-nitride materials generally crystallize in the wurtzite structure. In GaN, the c/a ratio is equal to 1.626 (Bernardini 2007), whereas its value for the ideal wurtzite structure is 1.633 (Morawiec, Sarzała, and Nakwaski 2013), where a and c are the lattice constants in the directions parallel and perpendicular to the c plane, respectively. Therefore, the GaN crystal is compressed in the c direction. Due to the resulting lack of inversion symmetry, as well as the partially ionic nature of the Ga-N bonds, group-III nitrides contain a nonzero spontaneous polarization P_{SP} along the c axis. Also, in III-nitride heterostructures, the lattice mismatch between the template and the active region induces elastic strain and mechanical stress that results in a piezoelectric polarization P_{PZ}. The total polarization in each layer is the sum of the spontaneous and piezoelectric components. The existence of polarization fields leads to band bending and results in the quantum confined Stark effect in c-plane oriented nitride QWs, which causes a decrease in interband oscillator strength and a voltage-dependent, red-shifted emission wavelength (Tian et al. 2013; Wu et al. 2013). Strain-induced polarization effects in nitride layers grown on semi-polar and non-polar templates have been theoretically investigated in several studies (A E Romanov, Baker, Nakamura, Speck, and Group 2006; J. S. Speck and S. F. Chichibu 2009; Young et al. 2012a; Haeger et al. 2012; A E Romanov, Baker, Nakamura, Speck, Jst, et al. 2006; Feezell et al. 2013; Young et al. 2012b).

4.2.1 Semipolar GaN Plane free-standing GaN Modeling

Traditionally, III-nitride devices are grown along the c-axis. Planes parallel to this axis (i.e., perpendicular to the c-plane) are electrically neutral since they have the same number of anions and cations, and therefore are called nonpolar. Planes oriented between the c- and any non-polar axis are called semi-polar. A crystallographic plane may be defined by the angle θ between the crystallographic c direction and the axis perpendicular to the plane, as shown in Figure 4.1. The plane of interest in this work, the $(20\bar{2}\bar{1})$ semi-polar plane, has an inclination angle θ with respect to (0001) of 75°.

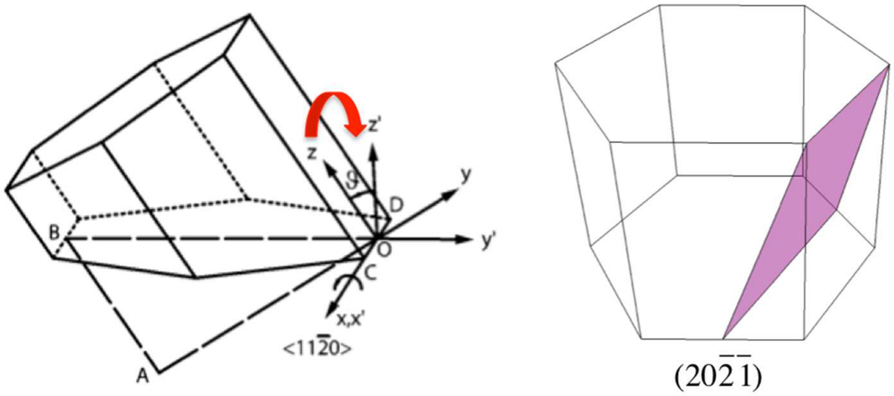

Figure 4.1 (a) Orientation of a generic semi-polar GaN plane and its inclination. (b) (20-2-1) semi-polar plane direction.

In this study, I have designed a III-nitride QWIP structure with detection wavelength of 32 μm (40 meV) to be grown on the $(20\bar{2}\bar{1})$ semi-polar plane, based on the theory described by Romanov (A E Romanov, Baker, Nakamura, Speck, J, et al. 2006). The results presented below show that by growing nitride devices along this $(20\bar{2}\bar{1})$ crystallographic orientation, one can produce QW structures with much reduced internal polarization fields. To compute the polarization fields in non-c-plane nitrides, one needs to rotate the coordinate system and go from natural (x, y, z) to prime (x', y', z') coordinates as shown in Figure 4.1(a). Here the coordinate system is rotated such that z' points along the growth direction. In the natural coordinate system, z is in the [0001] direction (i.e., the c direction) of the wurtzite crystal structure, while x and y are in the basal plane. When a thin layer is hetero-epitaxially grown on a template, it is constrained in such a way that it mimics the crystallographic orientation of the thick template. As a result, the strain parameters become inclination-angle dependent as follows

$$\varepsilon_{m1} = \frac{a_T - a_L}{a_L} \quad (4.1)$$

$$\varepsilon_{m2} = \frac{a_T c_T - \sqrt{(a_L c_T)^2 \cos^2\theta} + (a_T c_L)^2 \sin^2\theta}{\sqrt{(a_L c_L)^2 \cos^2\theta + (a_T c_L)^2 \sin^2}\theta} \quad (4.2)$$

where a_L and c_L (a_T and c_T) are the equilibrium lattice constants of the thin layer (template). The spontaneous and piezoelectric polarization fields of the epitaxial layer can then be computed as follows:

$$P'_{PS} = P_{PS}\cos\theta \quad (4.3)$$

$$P'_{PZ} = e_{31}\cos\theta \quad (4.4)$$

$$+\left(e_{31}\cos^3\theta + \frac{e_{33} - e_{15}}{2}\sin\theta\sin2\theta\right)\varepsilon_{y'y'} \quad (4.5)$$

$$+\left(\frac{e_{33} + e_{15}}{2}\sin\theta\sin2\theta + e_{33}\cos^3\theta\right)\varepsilon_{z'z'} \quad (4.6)$$

$$+[(e_{31} - e_{33})\cos\theta\sin2\theta + e_{15}\sin\theta\cos2\theta]\varepsilon_{y'z'} \quad (4.7)$$

$$P'_{TOTAL} = P'_{SP}\cos\theta + P'_{PZ} \quad (4.8)$$

More details about this calculation can be found in (Alexey E Romanov et al. 2011; A E Romanov, Baker, Nakamura, Speck, Jst, et al. 2006).

4.2.2 Device Design

In the present work (Durmaz et al. 2016), I have developed a Schrodinger-equation solver for the modeling of QWs grown along any arbitrary direction. This Schrodinger-equation solver includes spontaneous and piezoelectric polarizations effects based on the theory just described (A E Romanov, Baker, Nakamura, Speck, and Group 2006) to compute the conduction-band diagram of the QWIP active material under bias. Using this simulation code, I have developed the $(20\bar{2}\bar{1})$ GaN/AlGaN QWIP shown in Figure 4.2. The active material of this device consists of 30 GaN/$Al_{0.06}Ga_{0.94}N$ QWs embedded between a GaN template and a 200-nm-thick $Al_{0.04}Ga_{0.96}N$ cap layer. The well and barrier thicknesses are 67 and 115 Å, respectively, as determined from X-ray diffraction data analysis. The template, cap, and well layers are all *n*-doped with Si to a nominal level of 1×10^{18} cm^{-3}.

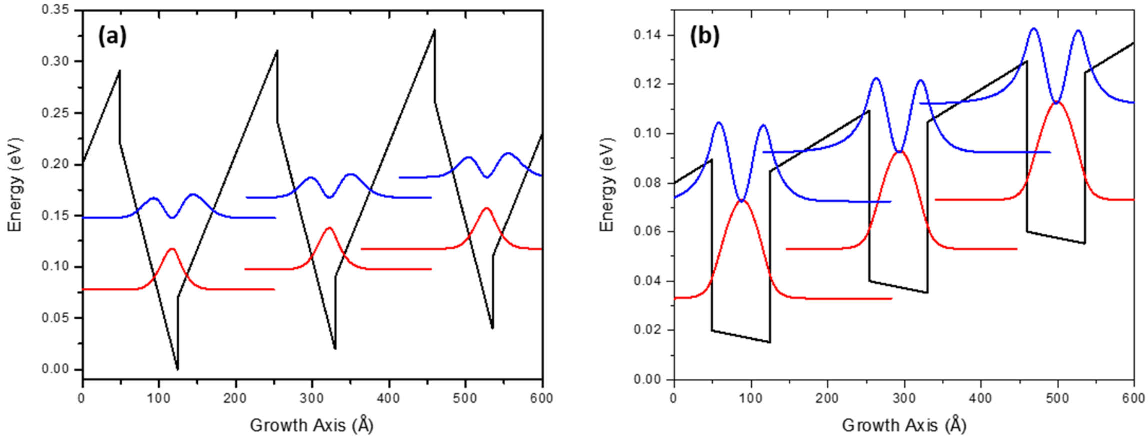

Figure 4.2 Conduction-band lineup of the semi-polar GaN/AlGaN QWIP developed in this work. The squared envelope functions of the bound-state subbands of each well are also shown, referenced to their respective energy levels. (a) Structure grown on the c-plane. (b) Structure grown on the $(20\bar{2}\bar{1})$ plane.

In Figure 4.2(a), I show the conduction-band lineup of the same QWIP structure if grown on the c-plane. In this case, both ground state and 1^{st}-excited state of each well are confined in the triangular portion of the QW potential energy profile. As a result, the 1^{st}-excited state is well below the top of the barriers, which is not desirable for detector performance since it leads to small escape probability and therefore limited responsivity, as discussed in section 2. These issues can be avoided by growing the same QWIP structure on the $(20\bar{2}\bar{1})$ plane, as shown in Figure 4.2(b). The internal electric fields produced by the interface polarization charges in these semi-polar QWs are approximately 16 and 9 kV/cm in the wells and barriers, respectively, i.e., an order of magnitude smaller than in the identical QWs grown along the *c* direction shown in Figure 4(a). These nonzero but relatively small internal fields are consistent with the large angle (75°) between the polar *c* axis and the $[20\bar{2}\bar{1}]$ growth direction. As a result, a fairly rectangular QW potential energy profile is obtained under zero-bias conditions. The calculated ISB transition energy in Figure 4.2(b) is 42.8 meV, corresponding to a frequency of 10.3 THz and a wavelength of 29.0 μm. By design the QW first-excited subbands are close to the top of the barriers, so as to optimize the tradeoff between strong ISB absorption and efficient escape of the photoexcited carriers out of the wells.

4.3 Device Growth and Characterization

The QWIP active material was grown by molecular beam epitaxy (MBE) on a single-side-polished 5×8 mm^2 $(20\bar{2}\bar{1})$ GaN substrate, using a Veeco GEN-II system with a UNI-Bulb RF plasma source for active nitrogen. Due to its non-standard size, the substrate is soldered to a 2-inch Si carrier wafer with In-Ga solder, and held in place with a Molybdenum spring plate. After thoroughly degassing at over 500 °C in a buffer vacuum chamber, the substrate is cleaned *in situ* by exposing it to a Ga beam equivalent pressure of 1.6×10^{-6} Torr for 1 hour while continuously ramping the substrate temperature up and down between 600 °C and 670 °C. These values were chosen so that at the low temperature Ga accumulates on the substrate and the reflection high-energy electron diffraction (RHEED) pattern is significantly dimmed or gone, while at the high temperature Ga evaporates from the substrate fast enough for the RHEED to fully brighten again before the next cycle. The plasma conditions are held constant throughout the growth, with a power of 300W and a nitrogen flow rate of 1.2 sccm, yielding a 5×10^{-7} Torr beam equivalent pressure of active nitrogen and an average AlGaN growth rate of around 275 nm/hour. Due to the high reactivity of Al, the Al/N flux ratio alone is used to control the alloy composition when growing AlGaN under Ga rich conditions.

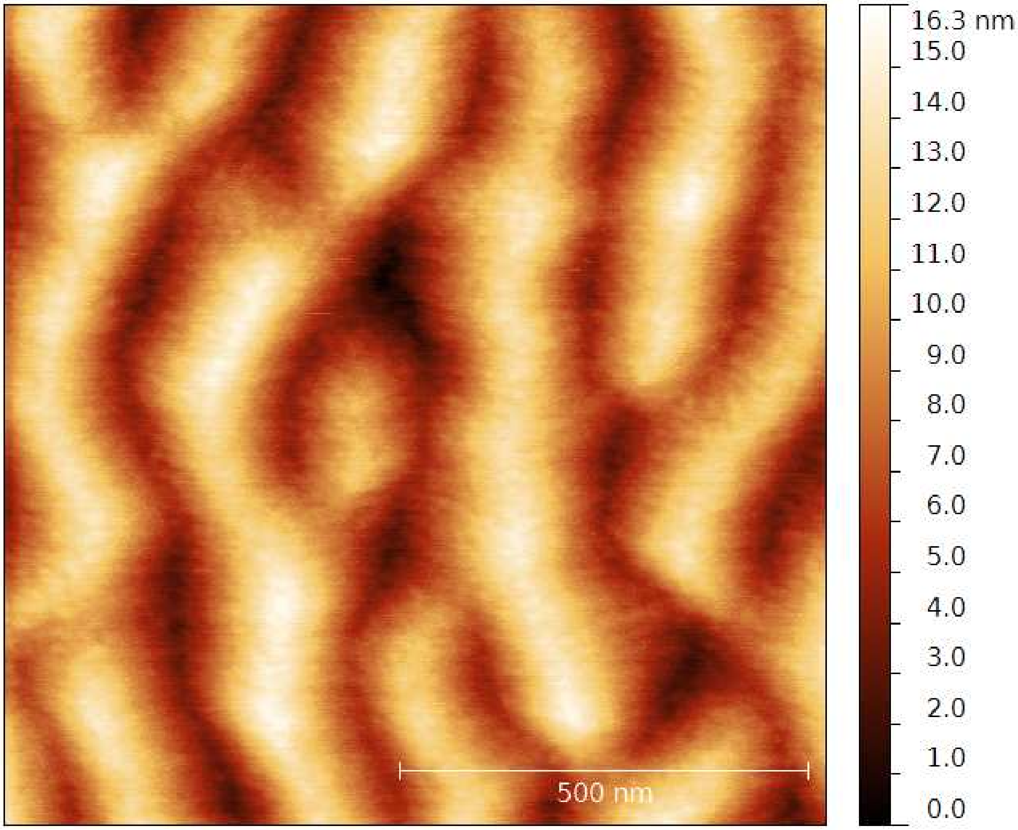

Figure 4.3 AFM surface profile of the epitaxial film.

AFM surface analysis was carried out with a Di3000 Picoforce system, and the average roughness of the epitaxial surface was found to be about 15-20 nm, as shown in Figure 4.3.

The sample photoluminescence properties were evaluated using a Photon Systems HeAg 224-nm pulsed laser with an average power of less than 1 mW. A primary emission peak is observed at 363 nm (3.42 eV), as shown in Figure 4.4, corresponding to the GaN substrate. An additional peak is also seen at 355.5 nm (3.49 eV), corresponding to the $Al_{0.04}Ga_{0.96}N$ cap layer.

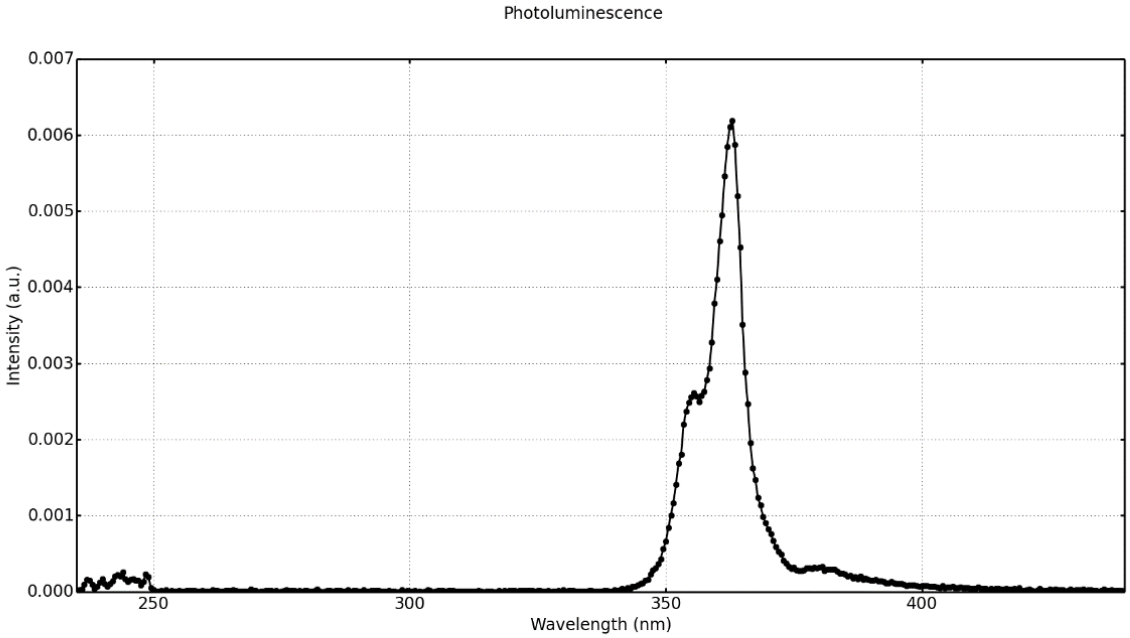

Figure 4.4 Photoluminescence spectrum of the epitaxial film. A primary peak is seen at 363 nm (3.42 eV) corresponding to the GaN substrate. An additional peak is observed at 355.5 nm (3.49 eV) corresponding to the $Al_{0.04}Ga_{0.96}N$ cap layer.

The structural quality of the epitaxial sample was characterized by high-resolution X-ray diffraction (HRXRD), using the copper $K_{\alpha 1}$ radiation line (λ= 0.15406 nm). Figure 4.5 shows the reciprocal space map around the GaN $(20\bar{2}1)$ reflection, acquired in a triple-axis configuration. The peak to the left is from the GaN substrate, while the peaks to the right are attributed to the GaN/$Al_{0.06}Ga_{0.94}N$ multiple-QW active region and the *n*-$Al_{0.04}Ga_{0.96}N$ cap. The satellite peaks from the active region indicate a periodicity of 182 Å.

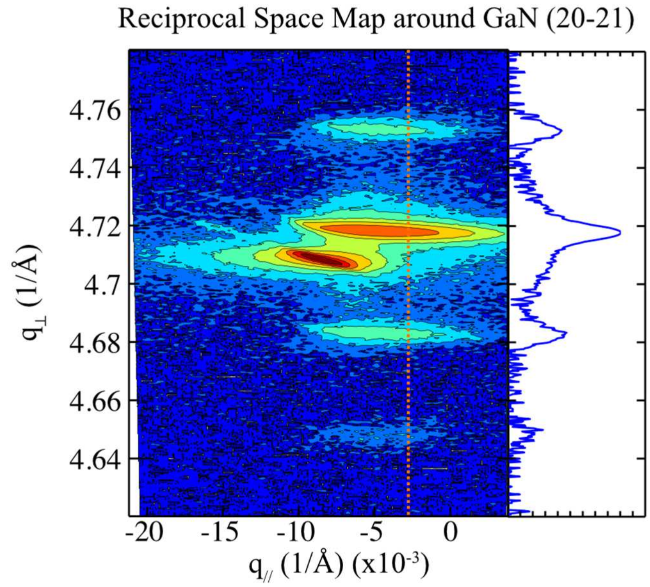

Figure 4.5 Reciprocal space map around the GaN $(\mathbf{20\bar{2}1})$ diffraction peak, acquired with X-rays incident parallel to the $[\mathbf{10\bar{1}4}]$ projection. The line plot on the right of the map shows the intensity scan along the dotted line, which captures the main and satellite peaks of the periodic multiple-QW active region.

4.4 Device fabrication

The device fabrication process used in this work is same as described in Chapter 3.2, and can be summarized as follows. After sample growth, 400 × 450 μm^2 mesa-structure devices are fabricated using standard photolithography and chlorine-plasma-assisted reactive ion etching (to an etch depth of 900 nm), with an AZ-5214 photoresist used as the etching mask. Metal contacts consisting of a Ti/Al/Ti/Au multilayer film are then deposited on top of and around each mesa, with the top contacts patterned in the shape of one-dimensional gratings with 15-μm period and 50-% duty cycle. Once again, the function of the grating is to couple normally incident light into the QWs in a way consistent with the polarization selection rules of ISB transitions. This arrangement is necessary due to the relatively large background *n*-doping of the GaN substrate, which makes it highly opaque at THz wavelengths, and therefore prevents polarization-resolved transmission and photocurrent measurements with angled backside excitation. Finally, another metallization step is performed to create Ni/Au bonding pads, and the samples are annealed in a forming gas environment at 850 °C for 50 sec and N_2/H_2 (95% / 5%) at 600 °C for 2 minutes in order to passivate possible leakage paths on the mesa sidewalls.

4.5 THz QWIP Results

For the temperature-dependent measurements, the devices are finally mounted on the cold finger of a continuous-flow liquid-helium cryostat. Figure 4.6 shows the dark current-voltage (I-V) characteristics of a device at different heat-sink temperatures. These traces are qualitatively consistent with standard models of carrier transport in QWIPs, (H.C. Liu 2007) including the observation of a significant decrease in dark current with decreasing temperature, which indicates a large contribution from thermionic emission out of the QWs. The relative large magnitude of the measured dark current also suggests the presence of electrical leakage, likely due to structural defects in the active material. In addition, it should be noted that the doping density used in the QWs is relatively high for such long-wavelength QWIPs, which further increases the dark current. The I-V traces of Figure 4.6 are also relatively symmetric with respect to the bias polarity, which is consistent with the nearly rectangular shape of the QWs and the absence of substantial band bending due to intrinsic electric fields in these semi-polar III-nitride heterostructures.

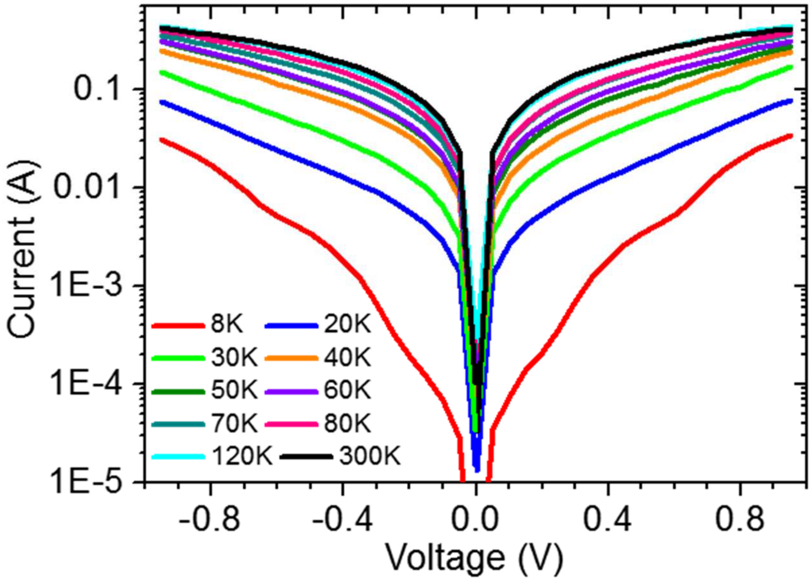

Figure 4.6 Temperature-dependent dark I-V characteristics.

The device photocurrent spectra were measured using a Bruker Vertex 70V Fourier transform infrared spectrometer (FTIR) equipped with a globar source and Mylar beamsplitter, via step-scan phase modulation and lock-in detection (more details of the measurement setup can be found in Section 3.4). The bias voltage and temperature dependence of the total photocurrent signal are presented in Figures 4.7(a) and 4.7(b), respectively. The behavior shown in Figure 4.7(a) is consistent with the bound-to-quasi-bound nature of the QWIPs under study. As the voltage is increased in either forward or reverse direction, the QW first-excited subbands (i.e., the quasi-bound states) become more strongly coupled to the adjacent continuum of unbound states, leading to an increase in the escape probability of the photoexcited carriers out of the wells. At the same time, the ISB absorption strength decreases due to the reduced confinement of the upper states. As a result, the photocurrent initially increases and eventually saturates with increasing bias voltage. As shown in Figure 4.7(b), the signal can be resolved up to a maximum temperature of about 50 K, which is reasonable for THz-range QWIPs (A.G.U. Perera et al. 2000; Graf et al. 2004b; Luo et al. 2005; Patrashin and Hosako 2008b).

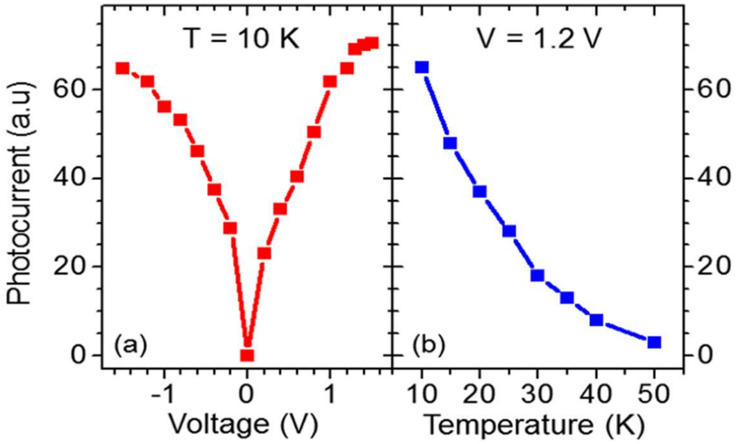

Figure 4.7 (a)) Photocurrent signal at a fixed temperature of 10 K measured as a function of applied voltage. (b) Photocurrent signal at a fixed bias voltage of 1.2 V measured as a function of heat-sink temperature.

The photocurrent spectrum of the same device at 10 K under an applied voltage of 1.2 V is shown in Figure 4.8. The photon energy of peak detection, obtained from a Gaussian fit of the experimental data, is 41.7 meV (i.e., 10.1-THz frequency and 29.7-µm wavelength), in excellent agreement with the calculated ISB transition energy of 42.8

meV shown in Figure 4.8. By comparing these data to similar measurement results obtained with a calibrated detector, the peak responsivity of the device of Figure 4.8 is found to be on the order of 10 mA/W. This value is on the low end of the range of responsivities reported with previously demonstrated GaAs/AlGaAs THz QWIPs (operating at longer wavelengths) (Perera et al. 2000; Graf et al. 2004a; Luo et al. 2005; Patrashin and Hosako 2008b). A somewhat smaller value (7 mA/W) was obtained with the *c*-plane III-nitride QWIP of ref. 12 (F. F. Sudradjat et al. 2012), based on the aforementioned double-step QW design. More importantly, the responsivity spectrum of Figure 4.8 also features a much narrower linewidth of 16.1 meV FWHM (versus 38.3 meV in ref. 12)(F. F. Sudradjat et al. 2012), indicative of reduced scattering from interface roughness and other defects and/or improved uniformity of the active QWs.

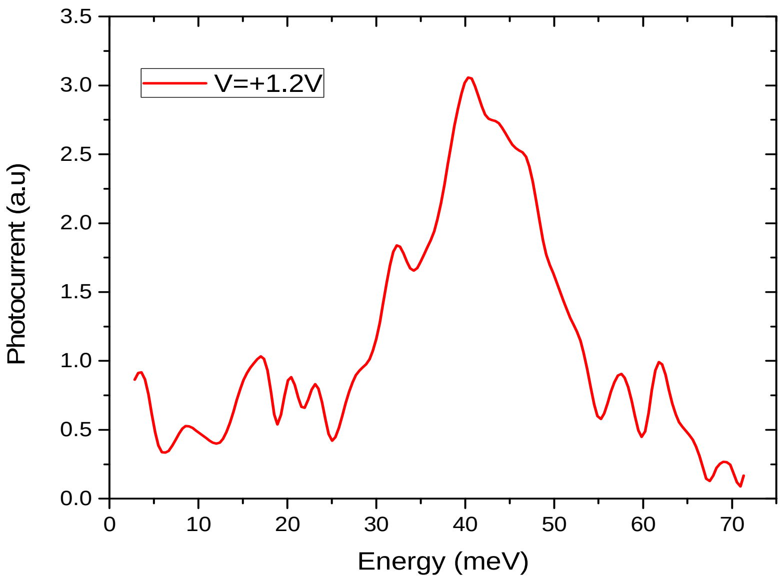

Figure 4.8 Photocurrent spectrum measured at 10 K under an applied voltage of 1.2 V.

These results therefore indicate that III-nitride QWs featuring the high structural quality required for ISB device applications can be developed on semi-polar $(20\bar{2}\bar{1})$ GaN substrates, with the additional important advantage of negligible polarization-induced internal electric fields. With further optimization of the growth process and active material design, we expect that high-performance QWIPs can be developed with these QWs, capable of operation across the entire THz range including the unavailable reststrahlen band of arsenide semiconductors. The same materials platform is also promising for the development of THz quantum cascade emitters, and the investigation of their expected advantages in terms of high-temperature operation.

5 FAR-INFRARED ISB ABSROPTION in SiGe QUANTUM WELLS NANO-MEMBRANES

In this thesis work, I have also considered the Si/SiGe materials system for the purpose of extending both the wavelength range and the operating temperature of THz devices. Si-based ISB devices generally make use of hole ISB transitions, since the valence-band (VB) offset in these QWs is larger than the conduction-band (CB) offset, so that holes experience more quantum confinement than electrons. As a result, the interaction between photons and holes becomes the relevant ISB absorption or emission mechanism. Due to their non-polar nature, these materials are free from reststrahlen absorption and resonant electron (or hole) / phonon scattering, unlike III-V semiconductors. Therefore, Si/SiGe QWs are promising candidate for high-temperature high-performance ISB device operation across the entire THz spectrum, with the additional advantage of direct integration with CMOS technology. Si/SiGe photodetectors and light emitters based on ISBTs have already been demonstrated (People et al. 1992; D. Krapf; P. Rauter 2011; Safina, Lazzari, and Said 2012; Matmon et al. 2010). Conventionally, these optoelectronic devices are grown pseudomorphically on Si substrates, and the maximum Ge content and number of QWs are limited by accumulation of strain due to the large lattice mismatch between Si and Ge. When the accumulated strain exceeds a certain threshold, it relaxes plastically through the formation of defects that are highly deleterious to device performance. In this work, we have demonstrated a novel nanomembrane (NM) strain engineering technique that consists of growing the QW active region on a released NM, whose lattice constant equals that of the overlaying heterostructure in its relaxed state (Sookchoo et al. 2013). By using this strategy, the fabrication of QW active regions that are free of threading dislocations is possible.

5.1 Device Design and Development

The Si/SiGe heterostructures developed in this work were designed and modeled based on the theory described in (Fromherz 1994), where the bound-state energies and eigenfunctions are computed with a self-consistent Schrodinger-Poisson equations solver based on a 6×6 Luttinger-Kohn model. The sample used to demonstrate ISB absorption in SiGe MQW NMs consists of 40 repetitions of 7-nm-thick $Si_{0.8}Ge_{0.2}$ wells and 33-nm-thick Si barriers. In order to minimize spectral broadening due to impurity scattering, modulation doping is employed, with a portion of each barrier layer doped p-type with boron. The sample layer thicknesses and alloy compositions were chosen to produce hole ISB absorption near 60 meV, and are summarized in Figure 5.1.

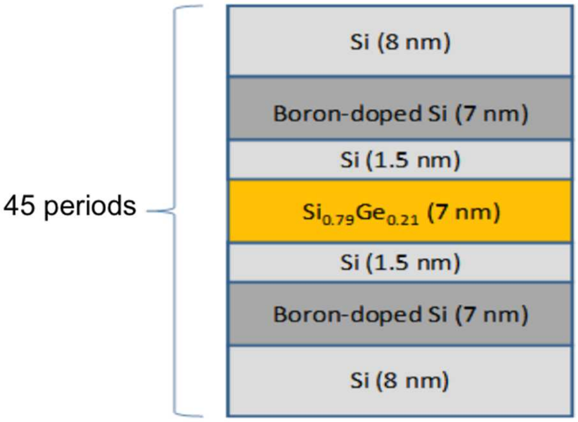

Figure 5.1 Schematic cross-section of the Si/SiGe QWs studied in this work.

5.2 Fabrication Process

The fabrication flow of this structure is shown in Figure 5.2 and has been carried out by our collaborators at the University of Wisconsin-Madison (Prof. Lagally's group) (Sookchoo et al. 2013). First, a thin epilayer consisting of only 5 QW periods is grown on a suitably thinned Si template layer of a Silicon on Insulator (SOI) substrate, using low-pressure chemical vapor deposition (LPCVD) with silane, germane, and diborane precursors. The resulting epitaxial film can be expected to be fully pseudomorphic with respect to the Si template layer due to its small thickness well below the critical threshold for plastic relaxation.

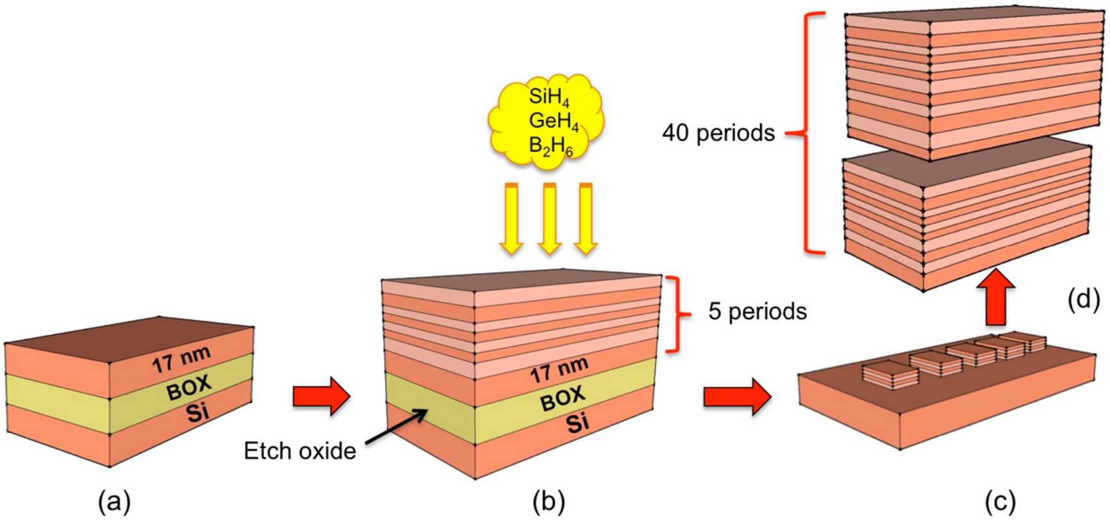

Figure 5.2 (a)-(d) Schematic process flow for the development of strain compensated SiGe QW NMs.

Next, the SOI buried-oxide (BOX) layer is dissolved in a wet etch, resulting in the formation of a NM where the stress due to the lattice mismatch between Si and $Si_{0.8}Ge_{0.2}$ is elastically relaxed via strain sharing. Specifically, the compressive strain in the $Si_{0.8}Ge_{0.2}$ wells is partially relaxed through the introduction of tensile strain in the Si barriers, until the in-plane lattice constant reaches a final value that produces zero net strain per period. This behavior is confirmed in Figure 5.2(e): an upward shift of the SiGe peak is clearly observed in the XRD reciprocal-space map measured after NM release, which is consistent with compressive-strain relaxation in the SiGe layers.

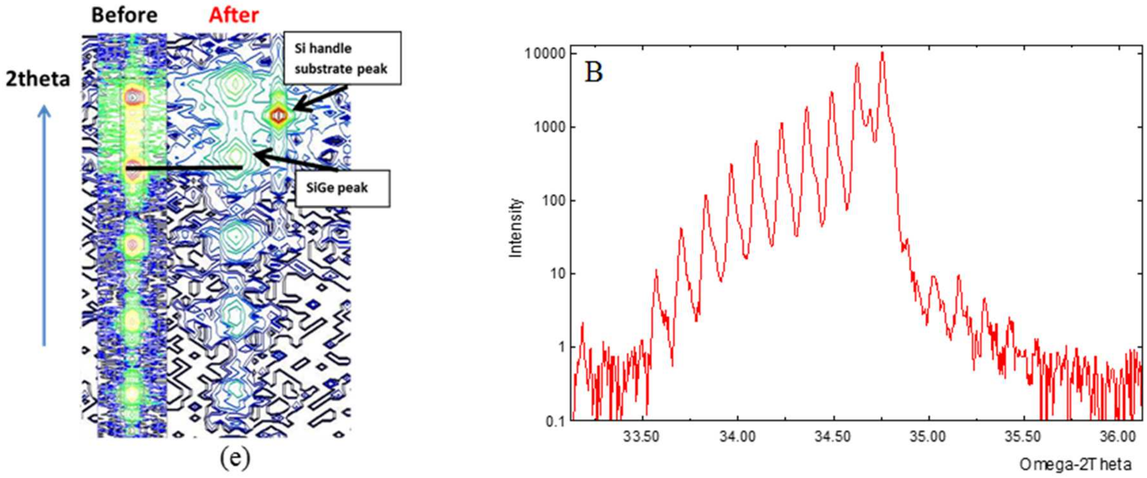

Figure 5.3 (a) XRD reciprocal-space maps of the initial 5-period SiGe/Si QW structure measured before and after release from the SOI substrate via wet etching of the BOX layer. (b) High-resolution XRD scan of a 45-period sample where the top 40 QWs were grown on a released NM.

After removal of the BOX layer, the NMs settle on the Si substrate where they are bonded with an anneal process. Finally, these NMs can be used for the strain-compensated growth of 40 additional QW periods. Since no net strain accumulates in these QWs, no plastic deformation leading to misfit dislocations is expected despite the large number of layers. As shown in Figure 5.3, HRXRD data measured with this sample feature sharp and uniformly spaced superlattice peaks, which indicate excellent crystalline quality.

5.3 Intersubband Absorption Spectroscopy

The ISB absorption spectra of the sample just described were measured using the FTIR spectrometer operated in rapid-scan mode and equipped with a Mylar beam splitter and a liquid-helium-cooled Si bolometer. For these measurements the sample input and output facets were lapped at 45◦ in order to enable TM-polarized photon absorption involving transitions between subbands HH1 and HH2 [as defined in the valence-band diagram of Figure 5.6(a) below]. During the measurements, light from the FTIR internal blackbody source is focused on the input facet of the sample using a beam condenser (producing a focused spot 6× smaller than the actual beam size), and the transmitted light is collected from the output facet and finally measured with the Si bolometer. A polyethylene polarizer is used in the optical path for polarization control.

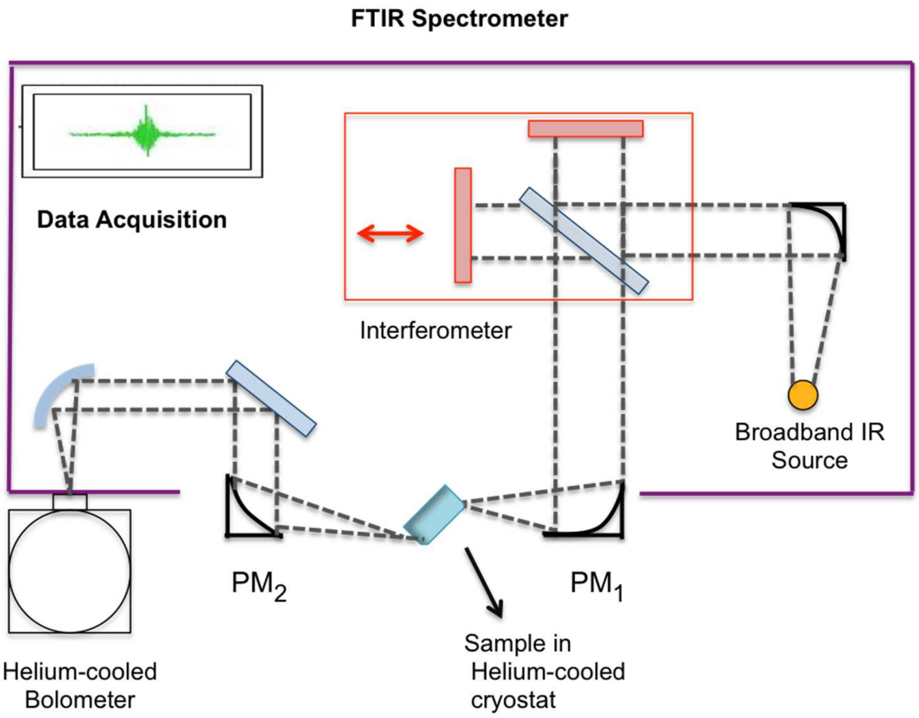

Figure 5.4 THz ISB absorption spectroscopy experimental setup

The absorption spectra were recorded at different temperatures and normalized to those of a nominally identical sample without QWs. A pronounced absorption peak is clearly observed at low temperatures, centered at a photon energy of about 64 meV, in good agreement with the calculated peak ISB absorption energy [58 meV, due to transitions between the lowest two heavy-hole (HH) subbands] as shown in Figure 5.6 (b). As illustrated in this figure, the absorption strength decreases with increasing temperature due to thermal population of the excited subbands. No similar absorption peak was measured with TE-polarized incident light, consistent with the polarization selection rules of HH ISB transitions. Finally, a similar QW structure was grown on bulk Si under the same conditions and measured with the same method. As shown in Figure 5.6(c), the QWs grown on NMs show a substantially stronger and narrower absorption spectrum compared to the QWs grown on bulk Si. The spectral width of the QW-NM ISB absorption spectrum (15 meV) also compares favorably with previous measurements from similar Si/SiGe QWs grown on bulk Si substrates (over 20 meV) (Pornstatit et al. 2013). Therefore, these results are very promising for far-infrared ISB device applications based on Si quantum structures.

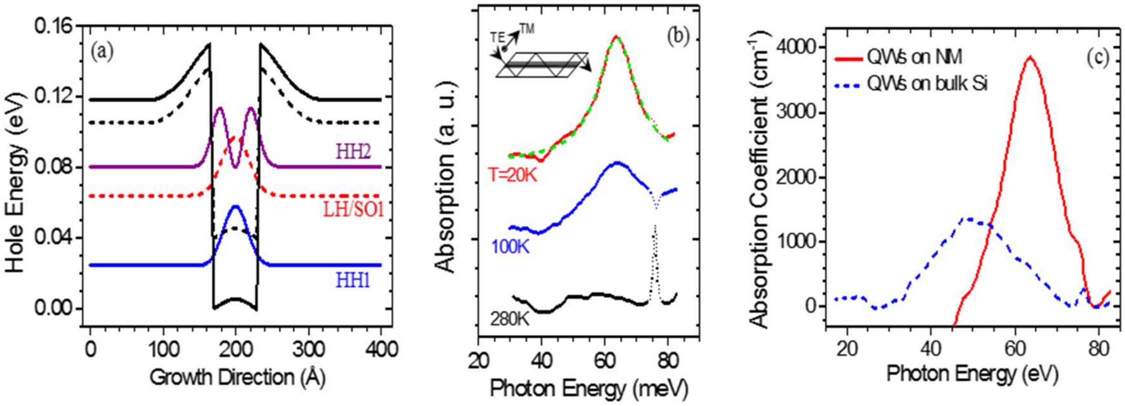

Figure 5.5 Figure 5.6 (a) Valence-band diagram of the QW structure developed in this work (b) TM-polarized inverse transmission spectra measured at different temperatures. The narrow features near 76 meV are attributed to phonon absorption processes. Inset: experimental geometry. (c) Low-temperature absorption spectrum of the same sample (solid line) and of a similar QW structure grown on a Si substrate (dashed line).

6 SiGe NANOMEMBRANE QUANTUM-WELLS INFRARED PHOTODETECTORs (QWIPS)

6.1 Motivations

Silicon, germanium, and related alloys have provided the leading materials platform of microelectronics for the past several decades. More recently, the development of optoelectronic devices based on these group-IV semiconductors has also become the subject of extensive research efforts, with the general goal of enabling the large-scale on-chip integration of electronic and photonic functionalities in a CMOS compatible process. The use of silicon photonics for data communications at fiber-optics transmission wavelengths is already entering commercialization. At the same time, group-IV semiconductor devices operating at longer wavelengths (into the mid- and far-infrared spectral regions) are currently being explored for the development of highly integrated systems for biochemical sensing and thermal imaging (Richard Soref 2010). While Si and Ge are transparent over a wide portion of the mid/far-infrared spectrum, they can be used for active optoelectronic devices at the same wavelengths based on intersubband (ISB) transitions in quantum wells (QWs) (Paiella 2006).

Early work in this context has focused on SiGe QWIPs (R. P. G. Karunasiri, Park, and Wang 1991; Park, Karunasiri, and Wang 1992; People et al. 1992; P. Kruck 1996; D. Krapf 2001; P. Rauter 2009; P. Rauter 2011), i.e., the type of unipolar photoconductive devices described in Chapter 2. Intersubband electroluminescence has also been reported (Dehlinger et al. 2000; Bormann et al. 2002; Lynch et al. 2002; Diehl et al. 2002; Bates et al. 2003) following several theoretical proposals (Sun, Friedman, and Soref 1995;

Friedman, Soref, and Sun 1998), as a promising first step towards the demonstration of SiGe QC lasers. As already mentioned, THz light emission is particularly significant in these group-IV semiconductors, owing to their nonpolar nature. Specifically, existing GaAs THz QC lasers are intrinsically limited to cryogenic operation and incomplete coverage of the THz spectrum, due to thermally activated ISB nonradiative decay and reststrahlen absorption caused by polar optical phonons (Williams 2007). In SiGe such electron-phonon and photon-phonon interactions are significantly weaker, so that in principle both limitations can be overcome. However, further progress in the development of group-IV ISB devices has so far been hindered by the large lattice mismatch (4.2 %) between Si and Ge and the resulting formation of extensive strain-induced defects in SiGe QWs. This issue is especially problematic in QC lasers, which require a large number of QWs with sufficiently different well and barrier compositions (i.e., sufficiently large band offsets) to provide strong quantum confinement for the upper laser subbands. When these structures are grown on rigid epitaxial substrates, the accumulated strain eventually relaxes plastically through the formation of misfit dislocations, causing severe degradation in the electrical and optical properties.

Following the initial work described in the previous chapter, here we investigate the use of lattice-matched substrates consisting of elastically relaxed NMs, as a way to address this strain accumulation problem for the growth of high-quality SiGe multiple-QW structures. Specifically, we report the development of a mid-infrared QWIP to illustrate how this approach can be effectively applied to electrically injected ISB devices. The NM substrate is fabricated by first growing a few periods of the desired

QW structure (with overall thickness well below the threshold for plastic deformation) on a Si-on-insulator (SOI) wafer. The resulting epitaxial film is then released to form a free-standing NM by etching the underlying SiO_2 layer. In the process, the internal stress due to lattice mismatch is relaxed via elastic strain sharing among the various layers. The end result is therefore a lattice-matched NM that can be used for the subsequent strain-compensated growth of an arbitrary number of identical QW periods without any strain accumulation. In the initial samples recently developed with this approach (Sookchoo et al. 2013), strong far-infrared ISB absorption spectra were measured with significantly narrower linewidth compared to similar QWs grown on rigid Si substrates [see Figure 5.5(c)], indicative of much improved materials quality.

An important question related to this fabrication process is how to achieve efficient vertical current injection into such ultrathin NMs. In typical multiple-QW devices, the active region is grown on a sufficiently thick (~ 100 nm or more) highly doped contact layer, which is then electrically addressed either through a conductive substrate or via etching and metallization from the top side. However, such contact layers cannot be incorporated in the NMs under study without at the same time impeding the elastic strain relaxation that is needed for the subsequent strain-compensated growth of the multiple-QW active region. The approach that we have developed to address this challenge is to transfer and bond the initial strain-relaxed NMs onto highly doped Si substrates, and then rely on charge transport across the NM-Si interface. In order to focus on the resulting electrical properties, in the present work this approach is investigated with a relatively simple ISB device structure, namely a SiGe mid-infrared QWIP. Our measurement results indicate that the bonded NM-Si interface allows for unobstructed current injection/extraction, and does not seem to affect the device characteristics in any significant way.

6.2 Device Design

The QWIP active-material design is illustrated schematically in Figure 6.1. Similar to most prior work on SiGe ISB devices, hole ISB transitions are employed in this structure due to the exceedingly small conduction-band offsets of SiGe/Si QWs (Paiella 2006). In passing, we note that electronic ISB transitions in the *L* valleys of Ge/SiGe QWs have also started to gain attention in recent years (Driscoll and Paiella 2006; Valavanis et al. 2011; Ortolani et al. 2011; Sabbagh et al. 2016), due to several potential advantages including larger oscillator strengths and longer nonradiative decay lifetimes. The development of these QWs has so far been hindered by the lack of high-quality SiGe substrates with sufficiently high Ge content, and therefore could also benefit strongly from the use of strain-relaxed NM substrates (initially grown on Ge-on-insulator wafers). The QWIP active material developed in the present work consists, nominally, of 4 nm-thick $Si_{0.73}Ge_{0.27}$ wells separated by 50-nm-thick Si barriers grown along the (001) direction. The first and last 2-nm-thick sections of each barrier (immediately adjacent to the neighboring wells) are doped *p*-type with boron to the level of 5×10^{18} cm^{-3}. The valence-band lineup of one period of this device structure under bias is shown in Figure 6.1, where E_{LH}, E_{HH}, and E_{SO} indicate the band edges of the light-hole (LH), heavy-hole (HH), and spin-orbit-split-off (SO) valence bands, respectively. Also plotted in the same figure are the squared envelope functions of the lowest HH and LH bound states referenced to their respective energy levels, which once again were computed using a 6×6 Luttinger-Kohn model (Fromherz 1994) coupled to a Poisson-equation solver.

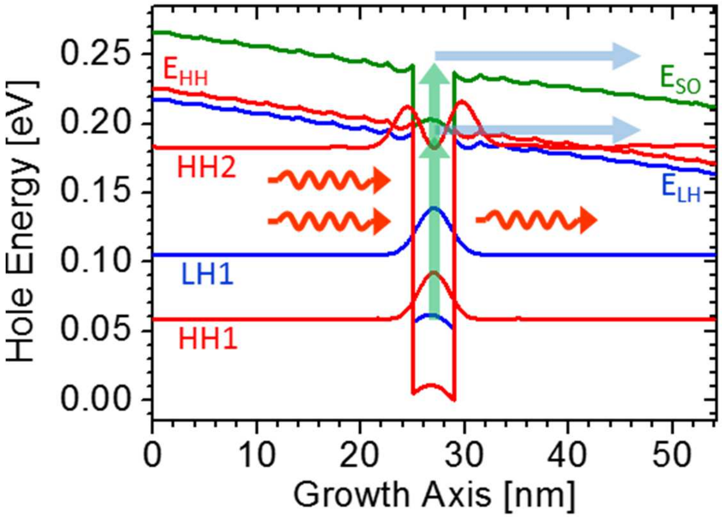

Figure 6.1 Calculated valence-band lineup of the QWIPs developed in this work, and squared envelope functions of the lowest-energy bound states. The arrows indicate the main mechanisms for photocurrent generation.

At the nominal doping level of this structure, a significant hole population is obtained in the ground-state subband of each QW (denoted HH1 in Figure 6.1). Photocurrent can then be produced via two distinct ISB absorption processes, indicated schematically by the arrows in the figure. First, holes can be promoted from HH1 into the first-excited HH subband (HH2), followed by tunneling into the continuum of unbound states over the adjacent barrier. These bound-to-bound transitions can only couple to TM-polarized light, following the aforementioned standard polarization selection rules of ISB absorption. The corresponding absorption peak is centered at a photon energy of 122 meV (i.e., at a wavelength of 10.2 μm) based on the simulation results of Figure 6.1. Second, holes can also be photoexcited from HH1 directly into the unbound HH and mixed LH/SO states over the barriers, through the absorption of light at sufficiently high photon energy. Such processes are not strongly polarization dependent, since they involve both ISB transitions between HH states (which are only allowed for TM light) and inter-valence-band transitions between HH and mixed LH/SO states (which have larger oscillator strength for TE light) (H. C. Liu and F Capasso 2000). The relative magnitude of these bound-to-bound versus bound-to-continuum contributions to the QWIP photocurrent depends on a well-known tradeoff (Schneider and Liu 2007): bound-to-bound transitions feature significantly larger absorption (due to the larger spatial overlap of the initial and final states), at the expense of reduced escape efficiency (since some of the photoexcited carriers in HH2 may fall back into the ground-state subband before tunneling out of the QWs).

6.3 Sample Growth and Device Fabrication

The samples developed in this work were grown by Pornsatit Sookchoo at University of Wisconsin-Madison (in the Lagally Research Group), using low-pressure chemical vapor deposition (LPCVD) with silane, germane, and diborane precursors, at a substrate temperature of about 700 and 600 °C for the Si and SiGe layers, respectively. The first step of the fabrication process involves the growth of a small number (three) of QW periods on the template layer of a (001) SOI wafer as shown in Figure 6.2(a). Because of its small thickness (and correspondingly small amount of accumulated strain), no inelastic strain relaxation is expected to take place in this heteroepitaxial film through the formation of misfit dislocations. Next, rectangular-shaped NMs consisting of the same film are completely released from the SOI handle wafer using well established techniques (Rogers, Lagally, and Nuzzo 2011). Specifically, the SOI buried oxide (BOX) layer is dissolved with a wet etch in a hydrofluoric acid (HF) solution, after the NM boundaries and a pattern of small holes are lithographically defined to facilitate etchant access to the BOX. As the NMs are released from the SOI substrate, their internal stress due to the lattice mismatch between Si and SiGe is elastically relaxed via strain sharing (Roberts et al. 2006; Rogers, Lagally, and Nuzzo 2011). In particular, the compressive strain in the SiGe well layers is partially relaxed through the introduction of tensile strain in the Si template and barrier layers, until the in-plane lattice constant reaches a final value that produces zero net strain per period.

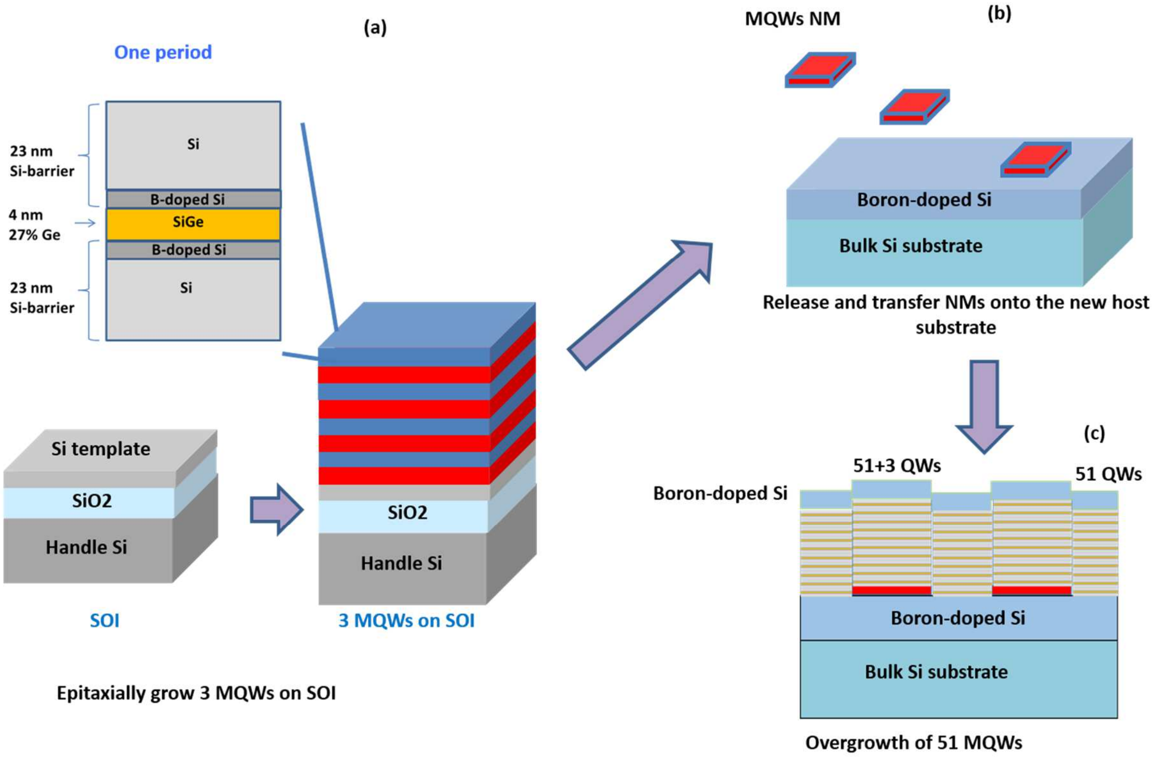

Figure 6.2 (a)-(c) Schematic process flow for the development of strain compensated SiGe QW NMs.

The resulting strain-relaxed NMs are then transferred and bonded onto a 500-nm-thick highly p-doped (~1×10^{19} cm^{-3}) Si contact layer previously grown on a separate Si substrate as shown in Figure 6.2(b). To that purpose, after the BOX has been fully dissolved in the wet etch, the SOI substrate is dipped in dimethylacetamide and then in deionized water to release the NMs, which are then transferred to the boron-doped Si substrate with a wet process. Prior to this step, a UV-ozone treatment is used to create a thin native oxide layer on the target substrate surface, and thus make it more hydrophilic so as to enable the transfer of large-area (i.e., a few mm^2) NMs without the formation of wrinkles. A 1-hour anneal at 450 °C is then used to improve the NM bonding to the Si contact layer. As shown by the measurement results presented below, the resulting interface is sufficiently conductive to produce devices with essentially the same electrical characteristics as otherwise identical samples grown epitaxially on the same contact layer.

Next, the surface is prepared for the subsequent growth with a mild cleaning procedure (consisting of 3 cycles of UV-ozone exposure and HF dipping) that avoids any NM peel-off. Finally, the Si substrate carrying the NMs is transferred back into the LPCVD chamber where 51 additional QW periods are grown under the same conditions as the initial 3 periods as shown in Figure 6.2(c). Because of the aforementioned elastic relaxation, the QWs grown on the NMs are fully strain compensated so that no net strain accumulates within each period. It should be noted that a similar arrangement could in principle be obtained with compositionally graded SiGe substrates (grown on bulk Si), which have also been investigated for the development of SiGe ISB devices (P.Rauter 2009; P. Rauter 2011; Diehl et al. 2003). However, these substrates suffer from a non-negligible density of threading dislocations, which are necessarily created during their growth (Gallas et al. 1999) and ultimately propagate into the overlaying epitaxial film. The strain-relaxed NM substrates under study are potentially free of such defects and therefore can provide higher structural quality, particularly for the growth of complex multiple-QW systems such as QC laser active materials.

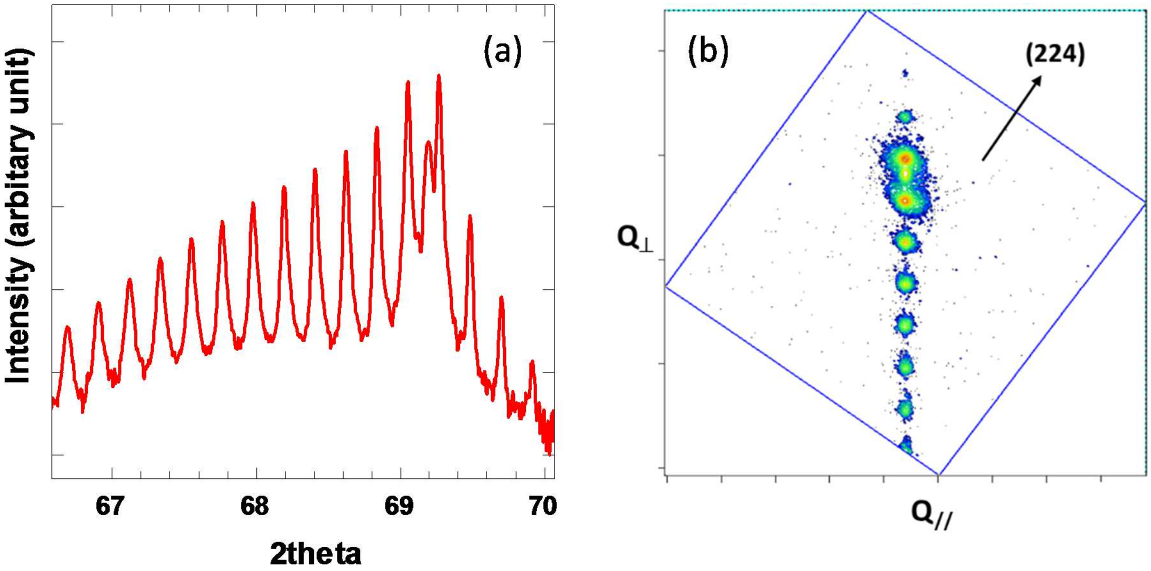

Figure 6.3 HRXRD data. (a) Omega/2theta scan along the (004) direction measured with sample A. (c) XRD reciprocal-space maps of the same sample measured along the (224) direction.

In the present work, two different QWIP samples (labeled A and B in the following) were developed with the procedure just described. Based on HRXRD data analysis, the well layer thickness of sample A is ~15% larger than the target value of Figure 6.1, whereas sample B is closer to specifications. The HRXRD data also indicate high crystalline quality of both materials, as illustrated in Figure 6.3. Specifically, Figure 6.3(a) shows an omega/2theta scan measured along the (004) direction in sample A. Many orders of sharp superlattice peaks are observed, indicative of excellent periodicity of the multiple-QW structure. A HRXRD reciprocal-space map of the same sample measured along the (224) direction is plotted in Figure 6.3(b), showing coherent film growth without plastic relaxation.

6.4 Electrical and Optical Characterization

For the photocurrent measurements, rectangular mesas with lateral dimensions of 300 to 400 μm are fabricated by reactive ion etching through the multiple-QW active material into the doped Si layer. Metal contacts consisting of a Ti/Au bilayer are then deposited on top of and around each mesa. The resulting device structure is shown schematically in Figure 6.4(a), together with a top-view optical micrograph. These devices were fabricated simultaneously on the QWs grown over the strain-relaxed NMs, and on the QWs grown over the nearby uncoated regions of the Si contact layer. The latter QWs are clearly not strain compensated since they are grown on a rigid unstrained Si lattice, and therefore allow for a direct comparison to ascertain the impact of the NM substrate on the QWIP characteristics.

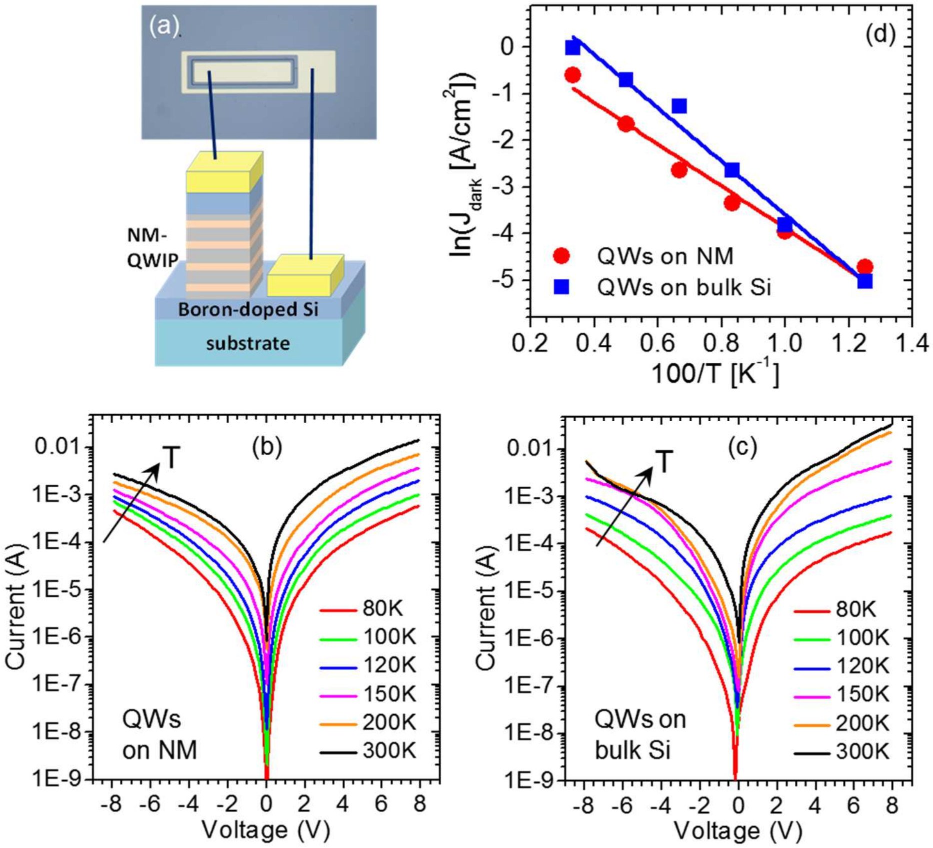

Figure 6.4 Electrical characterization results. (a) Schematic device structure (bottom panel) and top-view optical micrograph (top panel) of a QWIP developed in this work. (b) Temperature-dependent dark I-V characteristics of a 400×400-μm^2 device from sample B grown on a strain-relaxed NM. (c) Temperature-dependent dark I-V characteristics of a 400×300-μm^2 device from sample A grown directly on the Si contact layer. (d) Symbols: Arrhenius plot of the dark current density J$_{dark}$ from (b) and (c) at fixed bias voltage (2 V). Solid lines: linear fits.

Electrical data illustrating the best performance measured with both types of devices from both samples A and B are plotted in Figure 6.4. Figure 6.4(b) and 3(c) show the dark current-voltage (I-V) characteristics of, respectively, a device grown on a strain-relaxed NM and a device grown on the Si contact layer, for different heat-sink temperatures. The shapes of these traces are consistent with standard models of carrier transport in QWIPs (Schneider and Liu 2007), including the observation of a significant decrease in dark current with decreasing temperature. The slight asymmetry observed in both figures with respect to the bias polarity may be attributed to a small degree of doping migration, as previously reported with GaAs QWIPs (Liu et al. 1993). More importantly, the two devices of Figure 6.4(b) and 3(c) show very similar electrical characteristics, indicating that the bonded NM-Si interface of the former device essentially behaves like the homoepitaxial interface between the bottom QW barrier and the contact layer in the latter.

For a more detailed analysis, the symbols in Figure 6.4(d) show an Arrhenius plot of the dark current density J_{dark} of both devices at fixed bias voltage (2 V). Both traces are in good agreement with a linear fit (shown by the solid lines in the figure), indicating predominant thermal activation of the dark carrier transport. The activation energies inferred from the slopes of these linear fits are 39 and 49 meV for the NM- and Si-substrate device, respectively. Both values are significantly smaller than the effective barrier height $\Delta E = E_B - E_F$ (where E_F is the Fermi energy in each well and E_B is the HH band edge in the barrier downstream), which is computed to be 133 meV based on the simulation results of Figure 6.1. This discrepancy suggests that the carrier escape out of the QWs is not purely thermionic, and an additional transport mechanism dominates the temperature dependence of Figure 6.4(d). Given the location of the doping impurities in the present samples (in the first and last 2-nm-thick sections of each barrier), this additional mechanism is attributed to thermally activated tunneling through the acceptor impurity levels in the barriers. In any case, is should again be noted that the data shown in Figure 6.4(d) for the two types of devices are sufficiently similar to rule out any detrimental effect from the bonded NM-Si interface.

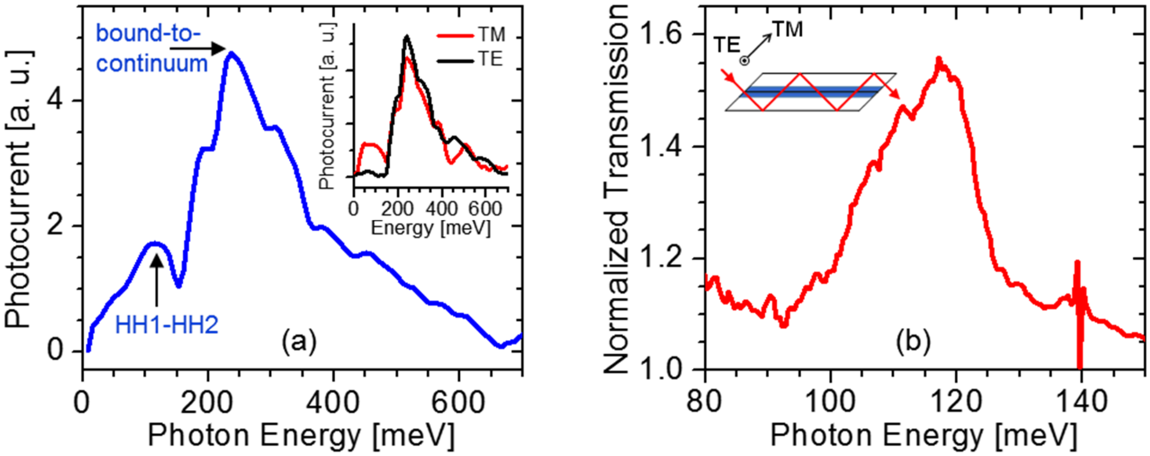

Figure 6.5 Optical characterization results. (a) Photocurrent spectrum of a 400×400-μm^2 device from sample A grown on a strain-relaxed NM, measured with unpolarized light. The heat-sink temperature and applied voltage are 80 K and 3 V, respectively. Inset: photocurrent spectra of the same device measured with TM- and TE-polarized light. (c) Ratio between the TE- and TM-polarized transmission spectra of an unprocessed piece of sample A at 80 K. Inset: experimental geometry used in this measurement.

The device photocurrent spectra were measured using a Fourier transform infrared spectrometer (FTIR) equipped with a globar source, via step-scan phase modulation and lock-in detection. In these measurements, the input light is coupled into the Si substrate at normal incidence through a facet lapped at 45º, and eventually reaches the QWIP mesa after a few bounces inside the substrate. This configuration allows probing the HH ISB transitions, which could not be excited by light incident along the mesa surface normal due to their TM polarization. Figure 6.5(a) shows the photocurrent spectrum of a NM device from sample A at 80 K under an applied voltage of 3 V, measured with unpolarized incident light. As indicated by the arrows, two distinct features can be identified in this spectrum peaked at about 238- and 115-meV photon energy, which are attributed to bound-to-continuum and HH1-HH2 ISB transitions, respectively. This assignment is consistent with the simulation results of Figure 6.1, where the HH1-HH2 transition energy is 122 meV, in close agreement with the peak photon energy of the long-wavelength photocurrent peak. At the same time, the short-wavelength peak extends over a broad range of energies above all the relevant barrier heights, and feature the characteristic asymmetric shape of bound-to-continuum transitions (Helm 2000).

As further evidence of this interpretation, in the inset of Figure 6.5(a) we show the photocurrent spectra of the same device under polarized illumination. The long-wavelength feature completely disappears if the input light has TE polarization (i.e., parallel to the plane of the QWs), consistent with the polarization selection rules of HH ISB transitions. In contrast, the short-wavelength feature is slightly weaker for TM input polarization (where the incident optical field is at 45° with respect to the growth axis), indicating significant contributions from inter-valence-band transitions between HH and mixed LH/SO states as well as ISB transitions between HH states. We have also measured the polarized transmission spectrum of an unprocessed sample from the same NM epitaxial material, using a multipass wedge geometry with two opposite facets lapped at 45°, as shown schematically in the inset of Figure 6.5(b). The results are shown in the same figure, where we plot the ratio between the TE- and TM-polarized transmission spectra at 80 K. The absorption peak due to HH1-HH2 ISB transitions is clearly resolved at a photon energy of about 117 meV, in excellent agreement with the photocurrent results of Figure 6.5(a). Finally, it should be noted that the relative strength of the bound-to-bound and bound-to-continuum contributions to the photocurrent depends not only on the aforementioned tradeoff between absorption strength and escape efficiency, but also on the wavelength-dependent transmission losses in the Si substrate. In particular, transmission measurements through this substrate indicate substantially larger absorption in the spectral vicinity of the HH1-HH2 transition energy, which can be ascribed to multi-phonon processes. The long-wavelength peak of Figure 6.5(a) is therefore significantly decreased compared to the bound-to-continuum feature.

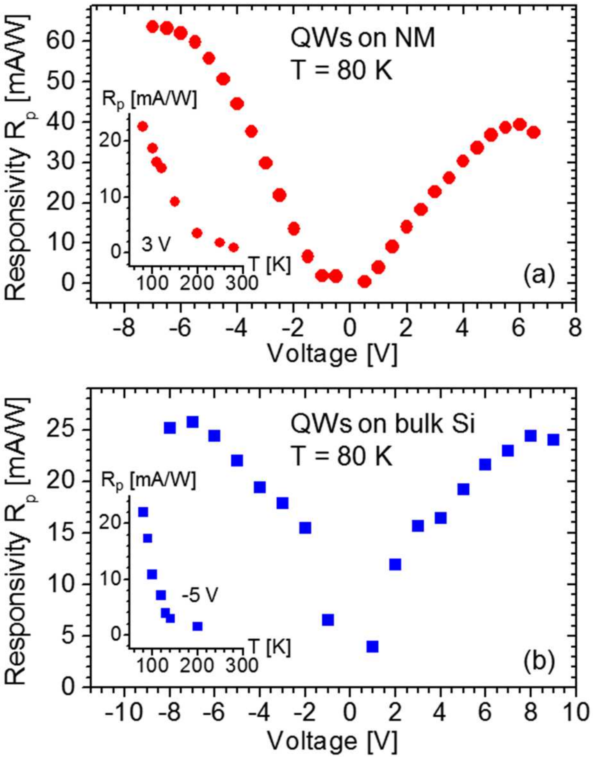

Figure 6.6 Measured peak responsivity of (a) the NM QWIP of Figure 6.5 and (b) a nearby device grown directly on the Si contact layer, plotted as a function of applied voltage for a heat-sink temperature of 80 K. The inset of each panel shown the peak responsivity of the corresponding device plotted as a function of temperature at fixed bias voltage.

Figure 6.6 summarizes our findings regarding the peak responsivity R_p of the QWIPs under study. This parameter was evaluated by repeating the same FTIR measurements with a calibrated InSb photodetectors, and then comparing the resulting photocurrent signal to the SiGe QWIP data at the photon energy of peak detection (near 5-μm wavelength). In Figure 6.6(a) we plot the peak responsivity of the device of Figure 6.5(a) at 80 K, as a function of bias voltage. The observed saturation in R_p with increasing voltage can be attributed to a concomitant saturation in drift velocity, as well as heating of the device active layer. As shown in the inset of Figure 6.6(a), the peak responsivity also decreases monotonically with increasing temperature, and can be resolved up to about 280 K. Figure 6.6(b) shows the same data measured with a nearby QWIP on the same chip, grown directly on the Si contact layer. These plots are again representative of the best performance observed with both types of devices from both samples A and B. The bulk-grown device of Figure 6.6(b) exhibits the same qualitative behavior as the NM QWIP of Figure 6.6(a). Its maximum responsivity, however, is noticeably smaller, by a factor of over 2, consistent with the expected improved structural quality of the strain-compensated QWs grown on the NMs. This result is also in agreement with the ISB absorption spectroscopy study of Figure 5.5(c) (Sookchoo et al. 2013), where a similar increase in peak absorption coefficient was measured in NM-grown SiGe/Si QWs relative to a nominally identical sample grown on a rigid Si substrate.

Finally, we note that the peak responsivity values plotted in Figure 6.6 are partly limited by optical absorption of the incident light during its multiple-bounce travel in the

Si substrate. The resulting attenuation factor can be estimated based on the measured normal-incidence transmission through the substrate at the wavelength of peak detection (~0.7 for a substrate thickness of 385 μm), combined with the distance between the QWIP mesas and the lapped facet (~ 1 mm). With this procedure, we find that the measured responsivities are reduced by a factor of 3-4 for both devices of Figure 6.6 due to such absorption. Therefore, maximum values of R_p of about 200 mA/W are possible with the NM devices under study with a more efficient input light coupling. In any case, the results of Figure 6.6 are comparable with prior demonstrations of SiGe/Si QWIPs (R. P. G. Karunasiri, Park, and Wang 1991; R P G Karunasiri, Park, and Wang 1992; People et al. 1992; P.Kruck 1996; Krapf et al. 2001; P.Rauter 2009; P. Rauter 2011), where responsivities ranging from a few mA/W to a few hundred mA/W are reported. It should also be noted that all these prior devices were grown by molecular beam epitaxy, which generally provides superior control of the QW growth parameter.

CONCLUSIONS AND FUTURE DIRECTIONS

In this thesis work, I have developed and studied ISB photodetectors (QWIPs) operating in the mid-IR and THz spectral regions, based on two different types of semiconductor materials.

First, GaN/AlGaN QWIPs grown on a standard c-plane GaN substrate and based on specially designed double-step QWs were designed, fabricated, and characterized. It was shown that the internal electric fields of nitride QWs are partially eliminated with this design. Experimental results indicate that double-step III-Nitride QWs are promising for the development of THz detectors operating at frequencies where As-based QWIPs are not available.

In the second part of my thesis work, THz ISB photodetectors based on semi-polar GaN/AlGaN heterostructures were designed, fabricated, and characterized (using the same methods as in the previous work). These semi-polar GaN/AlGaN QWIPs feature negligible polarization-induced internal electric fields, and show improved performance compared to our previous work, particularly with respect to narrower responsivity spectra. This materials platform is also promising for the development of THz quantum cascade emitters, and the investigation of their expected advantages in terms of high-temperature operation.

In the third part of this work, high-quality Si/SiGe MQW samples were designed and developed, based on a novel NM strain engineering approach. With this method, multilayer Si/SiGe NMs with the desired in-plane lattice constant are formed as a template for the subsequent strain compensated growth of any arbitrary number of additional QWs. Our ISB absorption spectroscopy and HRXRD measurement results indicate high structural quality of the resulting QWs, compared to similar samples grown on rigid Si substrates. This method can also be applied to more complex periodic QW structures such as Si-based THz QCLs, which in turn would allow taking advantage of the nonpolar nature and intrinsic CMOS compatibility of the SiGe materials system for applications in THz photonics.

Finally, I have designed and developed mid-infrared Si/SiGe QWIPs grown on lattice-matched NM substrates, fabricated with the same strain engineering method just described. Our results show that these strain engineered NMs can be effectively used for the development of electrically injected ISB devices requiring a large number of QWs. Future efforts should be focused on applying this promising approach for design and development of THz QCLs.

APPENDIX

Si/SiGe NANO-MEMBRANE INTERSUBBAND LIGHT EMITTERS

In this dissertation work, Si/SiGe QWIPs have been developed based on strain engineered NMs, and our results indicate that efficient charge transport across the NM/substrate interface is achievable. As the next step in the development of THz ISB devices based on this approach, I have designed a QC structure for THz electroluminescence based on Si/SiGe QWs. These group-IV semiconductors are non-polar and as a result electron-phonon interactions are significantly weaker than in III-V materials. For this reason, SiGe THz QCLs could potentially operate at higher temperatures compared to existing arsenide devices. In addition, the non-polar nature of SiGe QWs would allow QCL operation across the entire THz spectrum, whereas III-V semiconductors are fundamentally precluded from emission within their Reststrahlen band. Therefore, these materials are perfect candidates to overcome the present lack of practical THz sources for applications in security screening, medical diagnostics, and manufacturing quality control. The intrinsic CMOS compatibility of group-IV ISB devices also makes them particularly attractive.

The work reported in Chapter 5 has shown the feasibility of high-quality Si/SiGe QWs grown on relaxed NMs without plastic deformation for any arbitrary number of QW periods, as needed for QCL applications. Here I present a THz light emitter design that can be grown based on the same strategy. Figure A 1 shows the valance band lineup of three periods of this structure under bias, together with the squared envelope functions of the relevant bound states. Intersubband emission in this device is mostly expected to originate from transitions between the HH 1st excited and the ground states, at about 43 meV (10.4 THz). Once again, these calculations are based on a self-consistent Schrodinger-Poisson equations solver based on a 6×6 Luttinger-Kohn model.

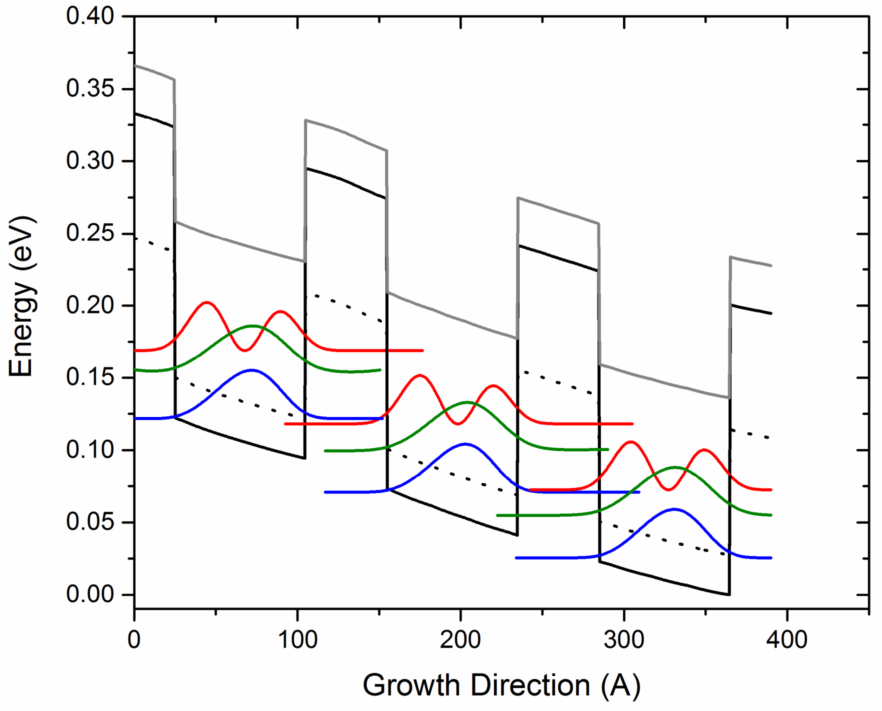

A 1 Valence-band diagram of the QW structure developed in this work

The active layer of Figure A1 consists of 8-nm-thick $Si_{0.80}Ge_{0.20}$ wells separated by 5-nm-thick Si barriers doped p-type to the level of $1x10^{17}$ cm^{-3}. The envelope functions shown in blue, green, and red are, respectively, the HH ground states, the LH ground states, and the HH 1st excited states. In the present design, carriers in the HH ground state of each well predominantly tunnel into to HH 1st excited state of the adjacent well downstream, and then can emit light through radiative decay into the HH ground state of the same well. Ideally, this cycle then continues through the entire active region.

This design is similar to prior reports of THz electroluminescence from Si/SiGe QWs (D.J. Paul, 2004; S.A. Lynch, 2002; R. Bates, 2003). However, we expect significantly improved emission efficiency resulting from the higher crystalline quality achievable with the strain engineered NMs developed in this thesis work.

BIBLIOGRAPHY

Arslan, Yetkin, Tahir Colakoglu, and Cengiz Besikci. 2013. “Diffraction-Grating-Coupled High Quantum Efficiency InP/InGaAs Quantum Well Infrared Photodetector Focal Plane Array.” *IEEE Journal of Quantum Electronics* 49 (2): 186–195.

Bates, R, S A Lynch, D J Paul, Z Ikonic, R W Kelsall, P Harrison, S L Liew, et al. 2003. “Interwell Intersubband *Applied Physics Letters.* 83 (20): 4092–4094.

Baumann, E., F. R. Giorgetta, D. Hofstetter, H. Lu, X. Chen, W. J. Schaff, L. F. Eastman, S. Golka, W. Schrenk, and G. Strasser. 2005. “Intersubband Photoconductivity at 1.6 μm Using a Strain-Compensated AlN⁄GaN Superlattice.” *Applied Physics Letters* 87 (19): 191102.

Bellotti, Enrico, Kristina Driscoll, Theodore D. Moustakas, and Roberto Paiella. 2008. “Monte Carlo Study of GaN versus GaAs Terahertz Quantum Cascade Structures.” *Applied Physics Letters* 92 (10): 101112.

Bernardini, F. 2007. *Nitride Semiconductor Devices: Principles and Simulation*. Wiley-VCH, Weinheim.

Bormann, I, K Brunner, S Hackenbuchner, G Zandler, G Abstreiter, K Brunner, S Schmult, and W Wegscheider. 2002. “Midinfrared Intersubband Electroluminescence of Si/SiGe Quantum Cascade Structures.” *Applied Physics Letters* 80 (13): 2260–2262.

Chamberlain, J. 1971. “Phase modulation in far infrared (submillimetre-wave) interferometers.” *Infrared Physics* (1): 25–55.

Chamberlain, J, and H A Gebbie. 1971. “Use of Phase Modulation in Submillimeter-Wave Interferometers.” *Applied Optics* 10 (5): 1184–1185.

Chamberlain, J.M. 2007. “Applied Terahertz Science: The Technology of the Future and Always Will Be?” In RE Miles et al. (eds.) *Terahertz Frequency Detection & Identification of Materials and Objects.* (pp. 341–352). Springer.

Dehlinger, G, L Diehl, U Gennser, H Sigg, J Faist, K Ensslin, D Grützmacher, and E Müller. 2000. “Intersubband Electroluminescence from Silicon-Based Quantum Cascade Structures.” *Science* 290: 2277–2279.

Diehl, L., S. Menteşe, E. Müller, D. Grützmacher, H. Sigg, U. Gennser, I. Sagnes, et al. 2003. “Electroluminescence from Strain-Compensated $Si_{0.2}Ge_{0.8}$/Si Quantum-Cascade Structures Based on a Bound-to-Continuum Transition.” *Applied Physics Letters* 81 (25): 4700–4702.

Driscoll, Kristina, and Roberto Paiella. 2006. “Silicon-Based Injection Lasers Using Electronic Intersubband Transitions in the L Valleys.” *Applied Physics Letters.* 89 (191110).

Durmaz, Habibe, Denis Nothern, Gordon Brummer, Theodore D. Moustakas, and Roberto Paiella. 2016. “Terahertz Intersubband Photodetectors Based on Semi-Polar GaN/AlGaN Heterostructures.” *Applied Physics Letters* (submitted).

Edmunds, C., J. Shao, M. Shirazi-Hd, M. J. Manfra, and O. Malis. 2014. “Terahertz Intersubband Absorption in Non-Polar M-Plane AlGaN/GaN Quantum Wells.” *Applied Physics Letters* 105 (2).

Faist, Jerome, Federico Capasso, Deborah L Sivco, Carlo Sirtori, Albert L Hutchinson, and Alfred Y Cho. 1994. “Quantum Cascade Laser.” *Science* 264 (5158): 553–556.

Feezell, Daniel F, James S Speck, Steven P Denbaars, and Shuji Nakamura. 2013. “Semipolar 2021 InGaN/GaN Light-Emitting Diodes for High-Efficiency Solid-State Lighting.” *Journal of Display Technology* 9 (4).

Foresi, J. S., and T. M. Moustakas. 1993. “Metal Contacts to Gallium Nitride.” *Applied Physics Letters.* 62 (22): 2859–2861.

Friedman, Lionel, Richard A Soref, and Gregory Sun. 1998. “Silicon-Based Interminiband Infrared Laser.” *Journal of Applied Physics* 83 (7): 3480–3485.

Fromherz, T., E. Koppensteiner, M. Helm, G. Bauer, J. F. Nützel, and Abstreiter. 1994. “Hole Energy Levels and Intersubband Absorption in Modulation-Doped Si/SiGe Multiple Quantum Wells.” *Physical Review B* 50: 15073–15085.

Gallas, B., J. M. Hartmann, I. Berbezier, M. Abdallah, J. Zhang, J. J. Harris, and B. A. Joyce. 1999. “Influence of Misfit and Threading Dislocations on the Surface Morphology of SiGe Graded-Layers.” *Journal of Crystal Growth* 201: 547.

Graf, Marcel, Giacomo Scalari, Daniel Hofstetter, Jérôme Faist, Harvey Beere, Edmund Linfield, David Ritchie, and Giles Davies. 2004a. “Terahertz Range Quantum Well Infrared Photodetector.” *Applied Physics Letters* 84 (4): 475–477.

Grossman, Erich, Charles Dietlein, Juha Ala-Laurinaho, Mikko Leivo, Leif Gronberg, Markus Gronholm, Petteri Lappalainen, Anssi Rautiainen, Aleksi Tamminen, and Arttu Luukanen. 2010. “Passive Terahertz Camera for Standoff Security Screening.” *Applied Optics.* 49 (19): E106–E120.

Haeger, Daniel A., Erin C. Young, Roy B. Chung, Feng Wu, Nathan A. Pfaff, Min Tsai, Kenji Fujito, et al. 2012. “384 Nm Laser Diode Grown on a ($202\bar{1}$) Semipolar Relaxed AlGaN Buffer Layer.” *Applied Physics Letters* 100 (16).

Hao, Mingrui, Shuai Zhang, Yueheng Zhang, Wenzhing Shen, Harald Schneider, and Huichun Liu. 2014. “Re-Examining the Doping Effect on the Performance of Quantum Well Infrared Photodetectors.” *Quantum Electronics Letters* 50 (1): 3–5.

Hassan, Ahmed M., David C. Hufnagle, Magda El-Shenawee, and Gilbert E. Pacey. 2012. “Terahertz Imaging for Margin Assessment of Breast Cancer Tumors.” In *2012 IEEE MTT-S International Microwave Symposium*, 1088. Piscataway, NJ: IEEE

Helm, M. 2000. “The Basic Physics of Intersubband Transitions,” *Semiconductors and Semimetals. 62*: 1–99.

Hofstetter, D, E Baumann, F R Giorgetta, J Dawlaty, P A George, F Rana, F Guillot, and E Monroy. 2008. “High Frequency Measurements on an AlN/GaN-Based Intersubband Detector at 1550 and 780nm High Frequency Measurements on an AlN/GaN-Based Intersubband Detector at 1550 and 780 Nm.” *Applied Physics Letters.* 92 (19): 231104–24701.

Hofstetter, D., S.S. Schad, H. Wu, W.J. Schaff, and L.F. Eastman. 2003. “GaN/AlN-Based Quantum-Well Infrared Photodetector for 1.55µm.” *Applied Physics Letters.* 83: 572–574.

Iizuka, N., K. Kaneko, and N. Suzuki. 2006. “Sub-Picosecond Modulation by Transition in GaN Quantum Wells.” *IEEE Journal of Quantum Electronics* 42: 765–771.

Karunasiri, R P G, J S Park, and K L Wang. 1992. “Normal Incidence Infrared Detector Using Intervalencesubband Transitions in $Si_{1-X}Ge_X$/Si Quantum Wells.” *Applied Physics Letters.* 61: 2434–2436.

Karunasiri, R. P. G., J. S. Park, and K. L. Wang. 1991. “Si1−xGex/Si Multiple Quantum Well Infrared Detector.” *Applied Physics Letters* 59: 2588–2590.

Kim, Jong Kyu, Ho Won Jang, and Jong-Lam Lee. 2002. “Mechanism for Ohmic Contact Formation of Ti on N-Type GaN Investigated Using Synchrotron Radiation Photoemission Spectroscopy.” *Applied Physics Letters.* 91 (11): 9214–9217.

Kotani, Teruhisa, Munetaka Arita, and Yasuhiko Arakawa. 2014. “Observation of Mid-Infrared Intersubband Absorption in Non-Polar M-Plane AlGaN/GaN Multiple Quantum Wells.” *Applied Physics Letters* 105 (26): 261108.

Krapf, D. et al 2001. “Infrared Multispectral Detection Using Si/Si_XGe_{1-X} Quantum Well Infrared Photodetectors.” *Applied Physics Letters.* 78 (4): 495–497.

Kruck, P. 1996. “Mediumwavelength, Normalincidence, P-type Si/SiGe Quantum Well Infrared Photodetector with Background Limited Performance up to 85 K.” *Applied Physics Letters.* 69 (22): 3372–3374.

Levine, B. F., K. K. Choi, C. G. Bethea, J. Walker, and R. J. Malik. 1987. “New 10 μm Infrared Detector Using Intersubband Absorption in Resonant Tunneling GaAlAs Superlattices.” *Applied Physics Letters.* 50 (16): 1092–1094.

Levine B. F. 1993. “Quantum-Well Infrared Photodetectors.” *Journal of Applied Physics* 74 (8): R1–R81.

Li, Yan, Anirban Bhattacharyya, Christos Thomidis, Theodore D. Moustakas, and Roberto Paiella. 2007. “Nonlinear Optical Waveguides Based on near-Infrared Intersubband Transitions in GaN/AlN Quantum Wells.” *Optics Express* 15: 5860–5865.

Lim, C B, A Ajay, C Bougerol, J Schörmann, M Beeler, J Lähnemann, M Eickhoff, and E Monroy. 2015. “Nonpolar M-Plane GaN/AlGaN Heterostructures with Intersubband Transitions in the 5 to 10 THz Band.” *Nanotechnology* 26 (43): 435201.

Lim, C. B., M. Beeler, A. Ajay, J. Lähnemann, E. Bellet-Amalric, C. Bougerol, and E. Monroy. 2015. “Intersubband Transitions in Nonpolar GaN/Al(Ga)N Heterostructures in the Short- and Mid-Wavelength Infrared Regions.” *Journal of Applied Physics* 118 (1): 014309.

Liu, H. C., Z. R. Wasilewski, M. Buchanan, and H. Chu. 1993. “Segregation of Si δ Doping in GaAs/AlGaAs Quantum Wells and the Cause of the Asymmetry in the Current/voltage Characteristics of Intersubband Infrared Detectors.” *Applied Physics Letters* 63: 761.

Liu, H. C. 1993. “Dependence of Absorption-Spectrum and Responsivity on the Upper State Position in Quantum-Well Intersubband Photodetectors.” *Journal of Applied Physics.* 73 (6): 3062.

Liu, H. C. and F Capasso. 2000. *Intersubband Transitions in Quantum Wells: Physics and Device Applications*. Academic Press.

Liu, H. C.. 2000. *Quantum Well Infrared Photodetector Physics and Novel Devices,.* Academic Press, London, UK.

Luo, H, HC Liu, CY Song, and ZR Wasilewski. 2005. “Background-Limited Terahertz Quantum-Well Photodetector.” *Applied Physics Letters.* 86 (23): 231103.

Lynch, S A, R Bates, D J Paul, D J Norris, A G Cullis, Z Ikonic, R W Kelsall, P Harrison, D D Arnone, and C R Pidgeon. 2002. “Intersubband Electroluminescence from Si/SiGe Cascade Emitters at Terahertz Frequencies.” *Applied Physics Letters.* 81 (9): 1543–1545.

Matmon, G, D J Paul, L Lever, M Califano, Z Ikoni, R W Kelsall, J Zhang, et al. 2010. “Si/SiGe Quantum Cascade Superlattice Designs for Terahertz Emission.” *Journal* *of Applied Physics* 107 (5): 1–8.

Miller, A J, A Luukanen, and E N Grossman. 2004. “Micromachined Antenna-Coupled Uncooled Microbolometers for Terahertz Imaging Arrays.” *Proceedings of SPIE* 5411: 8–24.

Morawiec, Seweryn, Robert P. Sarzała, and Włodzimierz Nakwaski. 2013. “A Method Used to Overcome Polarization Effects in Semi-Polar Structures of Nitride Light-Emitting Diodes Emitting Green Radiation.” *Applied Physics A* 113 (3): 801–809.

Motayed, A, R Bathe, MC Wood, OS Diouf, RD Vispute, and SN Mohammad. 2003. “Electrical, Thermal, and Microstructural Characteristics of Ti/Al/Ti/Au Multilayer Ohmic Contacts to N-Type GaN.” *Journal of Applied Physics* 93 (2): 1087–1094.

Palka, N. 2013. “Detection of Covered Materials in the TDS-THz Setup.” *Proceedings of SPIE. 8716:* 871608. doi: 10.1117/12.2015373

Ortolani, M., D. Stehr, M. Wagner, M. Helm, G. Pizzi, M. Virgilio, G. Grosso, G. Capellini, and M. De Seta. 2011. “Long Intersubband Relaxation Times in N-Type Germanium Quantum Wells.” *Applied Physics Letters.* 99: 201101.

Paiella, R. 2006. *Intersubband Transitions in Quantum Structures*. Mc-Graw-Hill.

Park, J S, R P G Karunasiri, and K L Wang. 1992. “Intervalencesubband Transition in SiGe/Si Multiple Quantum Wells−normal Incident Detection Lntervalence-Subband Transition in SiGe/Si Multiple Quantum Wells-Normal Incident Detection.” *Applied Physics Letters.* 61 (110): 681–683.

Patrashin, Mikhail, and Iwao Hosako. 2008a. “Terahertz Frontside-Illuminated Quantum-Well Photodetector.” *Optics Letters.* 33 (2): 168–170.

People, R., J. C. Bean, C. G. Bethea, S. K. Sputz, and L. J. Peticolas. 1992. “Broadband (8-14 μm), Normal Incidence, Pseudomorphic Ge_xSi_{1-x}/Si Strained-Layer Infrared Photodetector Operating between 20 and 77 K.” *Applied Physics Letters* . 61: 1122–1124.

Perera, A G U, S G Matsik, H C Liu, M Gao, M Buchanan, W J Schaff, and W Yeo. 2000. “GaAs/InGaAs Quantum Well Infrared Photodetector with a Cutoff Wavelength at 35 μm.” *Applied Physics Letters* 77 (5): 741–743.

Rauter, P. 2009. “SiGe Quantum Well Infrared Photodetectors on Pseudosubstrate.” *Applied Physics Letters.* 94:(081115).

Rauter, P. 2011. “Tensile Strained SiGe Quantum Well Infrared Photodetectors Based on a Light-Hole Ground State.” *Applied Physics Letters.* 98:(211106).

Roberts, Michelle M, Levente J Klein, Don E Savage, Keith A Slinker, Mark Friesen, George Celler, Mark A Eriksson, and Max G Lagally. 2006. “Elastically Relaxed Free-Standing Strained-Si Nanomembranes.” *Nature Materials* 5: 388–393.

Rogers, J. A., M. G. Lagally, and R. G. Nuzzo. 2011. “Synthesis, Assembly, and Applications of Semiconductor Nanomembranes.” *Nature* 477: 45–53.

Romanov, A E, T J Baker, S Nakamura, J S Speck, and Erato Jst Ucsb Group. 2006. “Strain-Induced Polarization in Wurtzite III-Nitride Semipolar Layers.” *Journal of Applied Physics* 100 (2): 23510–23522.

Romanov, Alexey E, Erin C Young, Feng Wu, Anurag Tyagi, Chad S Gallinat, Shuji Nakamura, Steve P Denbaars, and James S Speck. 2011. “Basal Plane Misfit Dislocations and Stress Relaxation in III-Nitride Semipolar Heteroepitaxy.” *Journal of Applied Physics* 109 (103522).

Ruvimov, S., Z. Liliental-Weber, and J. Washburn. 1996. “Microstructure of Ti/Al and Ti/Al/Ni/Au Ohmic Contacts for N-GaN.” *Applied Physics Letters.* 69 (11): 1556–1558.

Sabbagh, D., J. Schmidt, S. Winnerl, M. Helm, L. Di Gaspare, M. De Seta, M. Virgilio, and M. Ortolani. 2016. “Electron Dynamics in Silicon–germanium Terahertz Quantum Fountain Structures.” *ACS Photonics* 3: 403–414.

Sarusi, G., B. F. Levine, S. J. Pearton, K. M. S. Bandara, R. E. Leibenguth, and J. Y. Andersson. 1994. “Optimization of Two Dimensional Gratings for Very Long Wavelength Quantum Well Infrared Photodetectors.” *Applied Physics Letters.* 76 (4989-4994).

Scalari, G, C Walther, J Faist, H Beere, and D Ritchie. 2006. “Electrically Switchable, Two-Color Quantum Cascade Laser Emitting at 1.39 and 2.3 THz.” *Applied Physics Letters.* 88: 141102.

Scalari, Giacomo, Lassaad Ajili, Jérôme Faist, Harvey Beere, Edmund Linfield, David Ritchie, and Giles Davies. 2003. “Far-Infrared 87 Um Bound-to-Continuum Quantum-Cascade Lasers Operating up to 90 K.” *Applied Physics Letters.* 82 (19): 3165–3167.

Schneider, H., and H. C. Liu. 2007. *Quantum Well Infrared Photodetectors: Physics and Applications*. Springer-Verlag, Berlin.

Sfina, N., J.-L. Lazzari, and M. Said. 2012. “Si/$Si_{1-X}Ge_X$/Si-Based Quantum Wells Infrared Photodetector Operating at 1.55μm.” *Superlattices and Microstructures* 52 (4): 901–912.

Sookchoo, P, F Sudradjat, A Kiefer, H Durmaz, R Paiella, and Max G Lagally. 2013. “Strain Engineered SiGe Multiple- Quantum-Well Nanomembranes for

Applications.” *ACS Nano* 7 (3): 2326–2334.

Soref, R. 2010. “Mid-Infrared Photonics in Silicon and Germanium.” *Nature Photonics* 4: 495–497.

Speck J.S., and S. F. Chichibu. 2009. “Nonpolar and Semipolar Group III Nitride-Based Materials.” *MRS Bulletin* 34 (05): 304–312.

Sudradjat, Faisal F., Wei Zhang, Jeffrey Woodward, Habibe Durmaz, Theodore D. Moustakas, and Roberto Paiella. 2012. “Far-Infrared Intersubband Photodetectors Based on Double-Step III-Nitride Quantum Wells.” *Applied Physics Letters* 100 (24).

Sudradjat, Faisal, Wei Zhang, Kristina Driscoll, Yitao Liao, Anirban Bhattacharyya, Christos Thomidis, Lin Zhou, David J Smith, Theodore D Moustakas, and Roberto Paiella. 2010. “Sequential Tunneling Transport Characteristics of GaN/AlGaN Coupled- Quantum-Well Structures.” *Journal of Applied Physics* 108 (103704).

Sun, G., L. Friedman, and R. A. Soref. 1995. “Intersubband Lasing Lifetimes of SiGe/Si and GaAs/AlGaAs Multiple Quantum Well Structures.” *Applied Physics Letters* 66: 3425.

Sushil, Kumar, Wang I. Chun, Hu Qing, and L. Reno Joh. 2009. “Two-Well Terahertz Quantum-Cascade Laser with Direct Intrawell-Phonon Depopulation.” *Applied Physics Letters.* 95: 141110.

Suzuki, Nobuo, and Norio Lizuka. 1998. “Electron Scattering Rates in AlGaN/GaN Quantum Wells for 1.55-µm Inter-Subband Transition.” *Japanese Journal of Applied Physics* 37 (Par 2-No. 4A): L369–L371.

Tian, Wu, Wei-Yi Yan, Hui Xiong, Jian-Nan Dai, Yan-Yan Fang, Zhi-Hao Wu, Chen-Hui Yu, and Chang-Qin Chen. 2013. “Effects of Polarization on Intersubband Transitions of $Al_XGa_{1-X}N$/GaN Multi-Quantum Wells.” *Chinese Physics B* 22 (5): 057302.

Tonouchi, M. 2006. “Terahertz Technology.” *Nature Photonics* 1, 97–105. doi:10.1038/nphoton.2007.3

Valavanis, A, T V Dinh, L J M Lever, Z Ikoni, and R W Kelsall. 2011. “Material Configurations for N-Type Silicon-Based Terahertz Quantum Cascade Lasers.” *Physical Review B* 83(19). doi: 10.1103/PhysRevB.83.195321.

Vardi, A, G Bahir, F Guillot, C Bougerol, E Monroy, S E Schacham, M Tchernycheva, and F H Julien. 2008. “Near Infrared Quantum Cascade Detector in GaN/AlGaN/AlN Heterostructures Near Infrared Quantum Cascade Detector in GaN / AlGaN / AlN Heterostructures.” *Applied Physics Letters.* 92 (101): 11112–31103.

Walther, Christoph, Milan Fischer, Giacomo Scalari, Romain Terazzi, Nicolas Hoyler, and Jérôme Faist. 2007. “Quantum Cascade Lasers Operating from 1.2 to 1.6 THz.” *Applied Physics Letters.* 91 (13): 131122.

Williams, B. S. 2007. “Terahertz Quantum-Cascade Lasers.” *Nature Photonics* 1: 517.

Wu, F., W. Tian, W. Y. Yan, J. Zhang, S. C. Sun, J. N. Dai, Y. Y. Fang, Z. H. Wu, and C. Q. Chen. 2013. “Terahertz Intersubband Transition in GaN/AlGaN Step Quantum Well.” *Journal of Applied Physics* 113 (15): 1–8.

Young, Erin C, Feng Wu, Alexey E Romanov, Daniel A Haeger, Shuji Nakamura, Steven P Denbaars, Daniel A Cohen, and James S Speck. 2012a. “Compositionally Graded Relaxed AlGaN Buffers on Semipolar GaN for Mid- Ultraviolet Emission Compositionally Graded Relaxed AlGaN Buffers on Semipolar GaN for Mid-Ultraviolet Emission.” *Applied Physics Letters.* 101 (137): 124302–224703.

Young, Erin C, Feng Wu, Alexey E Romanov, Daniel a Haeger, Shuji Nakamura, Steven P Denbaars, Daniel a Cohen, and James S Speck. 2012b. “Compositionally Graded Relaxed AlGaN Buffers on Semipolar GaN for Mid-Ultraviolet Emission.” *Applied Physics Letters* 101 (14): 124302–224703.

Zhang, C. H., G. F. Zhao, B. B. Jin, Y. Y. Hou, H. H. Jia, J. Chen, and P. H. Wu. 2012. “Terahertz Imaging on Subcutaneous Tissues and Liver Inflamed by Liver Cancer Cells.” *Terahertz Science and Techonology* 5 (3): 114–123.

Zhang, R., X.G. Guo, C.Y. Song, M. Buchanan, Z.R. Wasilewski, J.C. Cao, and H.C. Liu. 2011. “Metal-Grating-Coupled Terahertz Quantum-Well Photodetectors.” *IEEE Electron Device Letters* 32 (5): 659–661.

CURRICULUM VITAE

HABIBE DURMAZ

durmazgul@gmail.com

EDUCATION

PhD in Electrical Engineering, 2016

Boston University, Boston MA

MS in Department of Physics, 2010

Temple University, Philadelphia PA

BS in Department of Physics, 2006

Selcuk University, Konya TURKEY

RESEARCH AND TEACHING

Boston University, Boston MA

Research Assistant (September 2013- May 2016)

- Development of semiconductor optoelectronic devices, such as light emitters and photodetectors in the MiR and FiR spectral region through the band gap engineering. Design of electronic band structures of the Quantum Well Infrared Photodetectors (QWIPs) based on group II-IV and III-V material systems and fabricate these devices. Electrical and spectroscopic characterization.
- Development of Graphene Plasmonics Photodetector: Fabrication, current-voltage (IV), and transmission measurements.
- Simulation, fabrication and characterization of dual-band perfect absorber for bio-sensing application.

Boston University, Boston MA

Teaching Assistant (May 2014-July 2014)

- Courses taught: “Photonics Lab”, “Electromagnetic Systems”

Temple University, Philadelphia PA

Research Assistant (September 2009-August 2010)

- Electrical characterization of carbon-nanotubes using Scanning Tunneling Microscopy (STM).

  Teaching Assistant (September 2008-August 2009)

- Courses taught: “Introduction to General Physics”, “Elementary Classical Physics”

ACADEMIC SKILLS

Clean room and fabrication skills:

Photolithography, e-beam lithography, mask design and writing for photolithography, Focus Ion Beam (FIB), e-beam evaporation, Reactive Ion Etching (RIE), Wire bonders.

Material Characterization Skills:

Scanning Electron Beam Microscopy (SEM), Atomic Force Microscopy (AFM), Scanning Tunneling Microscopy (STM,), Fourier Transform Infrared Spectroscopy (FTIR), ellipsometry, electroluminescence, photodetection, Current-Voltage measurement.

Computer Skills:

Matlab, LabVIEW, Mathematica, Nextnano, FDTD, Origin Pro, Igor, Autocad, LATEX, MS Office.

AWARDS AND FELLOWSHIPS

- Fellowship for M.S. and Ph.D studies in the USA (2007-2016)

  from Turkish Ministry of Education (MEB) based on a nationwide exam and GPA
- Fellowship for M.S. in Physics (2008-2010)

  from Temple University
- Dean's Honor/High Honor List at Selcuk University, Physics Department
- Fellowship for undergraduate studies (2002-2006)

PUBLICATIONS

Journal Articles (Published)

- P. Sookchoo, F. F. Sudradjat, A. M. Kiefer, **H. Durmaz**, R. Paiella, and M. G. Lagally, "Strain-Engineered SiGe Multiple-Quantum-Well Nanomembranes for Far-Infrared Intersubband Device Applications," in *ACS Nano* vol. 7, pp. 2326-2334, 2013

- F. F. Sudradjat, W. Zhang, J. Woodward, **H. Durmaz**, T. D. Moustakas, and R. Paiella, "Far-Infrared Intersubband Photodetectors Based on Double-Step III-Nitride Quantum Wells," in *Appl. Phys. Lett.*, vol. 100, art. no. 241113, . 2012

Submitted:

- **H. Durmaz**, D. Northern, G. Brummer, T. D. Moustakas, and R. Paiella, "Terahertz intersubband photodetector based on semi-polar GaN/AlGaN heterostructures," submitted App. Phys. Letts. 2016

Under Submission:

- **H. Durmaz**, P. Sookchoo, M. Lagally, and R. Paiella, "SiGe nanomembrane quantum-well infrared photodetectors," in *preparation*. (H.D. and P.S. are equally contributed)

Conference Presentations

- **H. Durmaz**, P. Sookchoo, F. F. Sudradjat, A. M. Kiefer, M. G. Lagally, and R. Paiella
  SiGe Nanomembrane Active Materials for Far-Infrared Intersubband Devices *OSA Topical Meeting on Integrated Photonics Research (IPR), paper IT3A.5* , Boston (MA), June 2015.

- F. F. Sudradjat, P. Sookchoo, **H. Durmaz**, A. M. Kiefer, M. G. Lagally, and R. Paiella
  Strain-Engineered SiGe Quantum-Well Nanomembranes for Far-Infrared Intersubband Device Applications *IEEE Conference on Lasers and Electro-Optics*, paper CW1O.5, San Jose (CA), June 2013.

- F. F. Sudradjat, W. Zhang, **H. Durmaz**, J. Woodward, T. D. Moustakas, and R. Paiella
  Far-Infrared Intersubband Photodetectors Based on GaN/AlGaN Double-Step Quantum Wells *International Conference on Intersubband Transitions in Quantum Wells*, paper XII-3, Bolton Landing (NY), Sept 2013.

- F. F. Sudradjat, P. Sookchoo, **H. Durmaz**, A. M. Kiefer, M. G. Lagally, and R. Paiella
  SiGe Multiple-Quantum-Well Nanomembranes for Far-Infrared Intersubband Devices *International Conference on Intersubband Transitions in Quantum Wells*, paper XIV-2, Bolton Landing (NY), Sept 2013.